https://doi.org/10.5194/egusphere-2026-4654
Preprint. Discussion started: 19 August 2026

Characterising the long-term effects of stratospheric aerosol injection geoengineering on the stratospheric ozone layer with mid-infrared limb emission sounding instruments

Mona Kosary[1], Pasquale Sellitto[1,2], Michael Höpfner[3], Bernd Funke[4], Alex Hoffmann[5], Jörn Ungermann[6], Quentin Errera[7], Simone Tilmes[8], Björn-Martin Sinnhuber[3]

[1]Univ. Paris-Est Créteil and Université de Paris Cité, CNRS, Laboratoire Interuniversitaire des Systèmes Atmosphériques, Institut Pierre Simon Laplace, Créteil, France
[2]Istituto Nazionale di Geofisica e Vulcanologia, Osservatorio Etneo, Catania, Italy
[3]Karlsruhe Institute of Technology, Institute of Meteorology and Climate Research (IMKASF), Karlsruhe, Germany
[4]Solar System Department, Instituto de Astrofísica de Andalucía, CSIC, Granada, Spain
[5]European Space Agency, EOP Climate Action, Sustainability and Science Department, European Space Research and Technology Centre (ESA/ESTEC), Noordwijk, The Netherlands
[6]Forschungszentrum Jülich, Institute of Climate and Energy Systems Stratosphere (ICE-4), Jülich, Germany
[7]Royal Belgian Institute for Space Aeronomy (BIRA-IASB), Brussels, Belgium
[8]Atmospheric Chemistry, Observations, and Modeling Laboratory, National Center for Atmospheric Research, Boulder, CO, USA

Correspondence to: Mona Kosary (mona.kosari@lisa.ipsl.fr)

Abstract. Stratospheric aerosol injection (SAI) has been proposed as a potential method to counteract anthropogenic greenhouse gas–driven global warming but it may perturb the stratospheric ozone layer. Here, we use existing SAI scenario simulations as pseudo-reality (PR) input to assess how a future mid-infrared limb-emission sounding observing system would characterise its modelled ozone response. Our PR scenarios were generated using CESM2(WACCM6) simulations following the SSP5-34-OS overshoot pathway, with and without SAI. Pseudo-observations (PO) of a future instrument, modelled around the satellite mission concept CAIRT (the Changing-Atmosphere Infra-Red Tomography explorer), were generated using mission performance simulators, providing full error propagation and spatial smoothing characteristics. Our results demonstrate that a CAIRT-like mission can monitor and quantitatively characterise global, regional and seasonal ozone impacts associated with this SAI scenario. The parent PR fields used here contain a modelled SAI-induced ozone response, including: a) a pronounced additional depletion of total column ozone in the southern hemispheric high latitudes, with austral springtime reductions exceeding 20 DU between 2033–2062, consistent with enhanced heterogeneous halogen activation on sulphate aerosols, b) a delay in Antarctic ozone recovery, and c) a moderate ozone increase in winter and spring at northern hemispheric mid and high latitudes, associated with altered transport and weakened subtropical jets. All these different decadal impacts of SAI interventions are observable with CAIRT PO and are fully distinguishable from a baseline non-SAI scenario. These findings highlight the importance of advanced satellite observations, which are not available nowadays, to monitor and evaluate these impacts.

https://doi.org/10.5194/egusphere-2026-4654
Preprint. Discussion started: 19 August 2026

1 Introduction

The Earth's atmosphere and climate system are undergoing substantial changes driven primarily due to anthropogenic emissions of greenhouse gases, pollutants, aerosols and their precursors, as well as ozone-depleting substances (ODSs). These human-induced changes overlay and outdo natural variability arising from factors such as volcanic eruptions and fluctuations in solar activity and dominate decadal-to-centennial scale climate trends (e.g., Legg, 2021; IPCC, 2023). Although it is now widely accepted that long-lived greenhouse gases, particularly CO_2, are the primary drivers of global climate change, substantial uncertainties remain in understanding climate dynamics on regional and annual-to-decadal scales. On these shorter timescales, regional climate responses are significantly influenced by atmospheric circulation and short-lived climate forcers, such as e.g., stratospheric water vapour, ozone, and aerosols (Solomon et al., 2010, 2011; Santer et al., 2014). Of particular importance are changes in the Upper Troposphere Lower Stratosphere (UTLS, ~10–25 km altitude), where variations in ozone, water vapour, and aerosols strongly influence surface climate through changes in temperature distribution, precipitation patterns, and other climate variables (e.g., Riese et al., 2012; Ridley et al., 2014). More generally, changes in stratospheric composition can have different impacts on the climate system. Alterations in stratospheric composition and circulation have wide-ranging implications for surface climate (e.g., Domeisen and Butler, 2020), weather patterns (Kidston et al., 2015) and air quality (Neu et al., 2014; Madronich et al., 2023). The UTLS and, more in general, the middle atmosphere is projected to experience significant compositional and dynamical changes in response to ongoing climate forcing.

Given the growing severity of climate risks, interest has increased in strategies to supplement traditional mitigation and adaptation efforts with geoengineering techniques (e.g., Crutzen 2006). Geoengineering approaches are receiving attention as potential tools to rapidly reduce global warming (e.g., Helwegen et al., 2019). These geoengineering methods are typically categorized into Carbon Dioxide Removal (CDR) and Solar Radiation Modification (SRM). First proposed in the 1960s, SRM encompasses techniques designed to reflect more sunlight back into space or facilitate the escape of infrared radiation. These methods could mitigate some climate risks, such as extreme temperatures and extreme precipitation events, but also carry significant uncertainties and potential unintended impacts on global and regional weather and climate patterns (e.g., Tilmes et al., 2016; Pinto et al., 2020). While mitigation and CDR strategies address the root causes of climate change by reducing atmospheric greenhouse gas concentrations, SRM targets surface temperature reduction through direct radiative interventions (Preston, 2013). However, SRM does not resolve the fundamental issue of greenhouse gas accumulation, nor does it mitigate related impacts such as ocean acidification (Russell et al., 2012). Among SRM techniques, Stratospheric Aerosol Injection (SAI) is currently the most extensively studied method. This involves injecting reflective aerosols, primarily sulphate aerosols (SA), or their chemical precursors, primarily sulphur dioxide (SO_2), into the stratosphere at altitudes around 20–25 km (Dykema et al., 2014) . Injections of SO_2 subsequently oxidise and nucleate into sulphuric acid droplets, enhancing the natural stratospheric aerosol loading, increasing the Earth's albedo in the solar spectral range and then reflecting more solar radiation, thus counterbalancing the decreased outgoing terrestrial radiation due to anthropogenic greenhouse gases emissions. Natural analogues of SAI are stratospheric volcanic eruptions. Recent volcanic eruptions, with injection into the stratosphere, such as

https://doi.org/10.5194/egusphere-2026-4654
Preprint. Discussion started: 19 August 2026

the 1991 eruption of Mount Pinatubo (McCormick et al., 1995) or the more recent 2022 eruption of the Hunga volcano (Sellitto et al., 2022), showed stratospheric aerosol layer increases with possible temporary global mean temperature reductions up to a few tenths of a degree, for Pinatubo, through large-scale SO_2 injections (e.g., Aubry et al., 2021). Despite its potential efficacy and relative cost-effectiveness, SAI can have severe unwanted effects. It can alter the stratospheric chemistry and dynamics, including changes in the ozone layer (Sofieva et al., 2026). A potential SAI deployment can also introduce significant socio-political risks. Societal risks include moral hazard—whereby SRM might weaken incentives for reducing essential greenhouse gas emissions (Qu and Silva, 2015)—as well as geopolitical concerns linked to unilateral deployment or misuse (Cherry et al., 2023). Additionally, the systematic and continuous injection required to reach the required sustained cooling presents the risk of a sudden termination ("termination shock"), potentially causing rapid and severe reversion to warming (Bronsther and Xu, 2025). Given these uncertainties and risks, robust international governance and comprehensive risk assessment frameworks are essential prerequisites before considering practical SAI deployment (Bellamy, 2025).

A key area of concern associated with SAI is its impact on the stratospheric ozone layer. Stratospheric ozone plays a critical role in protecting life on Earth by absorbing harmful ultraviolet-B (UV-B, 280–320 nm) radiation and influencing climate through radiative effects and feedbacks. Approximately 90% of atmospheric ozone resides in the stratosphere between roughly 10 and 50 km altitude (Cicerone, 1987). Anthropogenic emissions of long-lived halogenated compounds, notably chlorofluorocarbons, led to significant stratospheric ozone depletion during the second half of the 20th century. Polar stratospheric clouds (PSCs), common in both the Arctic and Antarctic winter, enable heterogeneous chemical reactions that activate halogens, catalysing ozone destruction each spring (Solomon et al., 1986). This results in the reoccurring so-called "ozone hole" over Antarctica. The persistent Antarctic polar vortex isolates and cools air masses, exacerbating ozone loss, conditions not typically matched in the Arctic, where ozone depletion is less extensive and more episodic (Tilmes et al., 2006; Müller et al., 2018). The discovery of the Antarctic ozone hole (Farman et al., 1985) prompted international action under the 1987 Montreal Protocol and subsequent amendments. As a result, emissions of ozone-depleting substances have sharply declined, initiating ozone layer recovery, projected to reach pre-1980 levels later this century (Bergesen et al., 2018). Nevertheless, stratospheric ozone continues to be sensitive to a variety of factors, including emissions of greenhouse gases (CO_2, CH_4, N_2O) (Eyring et al., 2010), volcanic (Tie and Brasseur, 1995) and wildfire-derived aerosols (Bernath et al., 2022), and solar variability (Bordi et al., 2015). A possible deployment of SAI could exacerbate stratospheric ozone destruction by increasing aerosol surface area density (SAD) in the stratosphere, facilitating heterogeneous chemical reactions like those after stratospheric volcanic eruptions (e.g., Solomon, 1999). Key catalytic cycles involving reactive chlorine (ClOx), bromine (BrOx), and hydrogen oxide (HOx) radicals are enhanced by increased SAD, while elevated water vapour can enhance HOx-driven ozone destruction, especially in the upper stratosphere (Fahey et al., 1993; Tilmes et al., 2018). These chemical and dynamical changes combine to alter ozone concentrations regionally and vertically. Additionally, sulphate aerosols absorb near- and mid-infrared radiation, warming the lower tropical stratosphere, altering circulation patterns such as the Brewer-Dobson circulation (Niemeier and Schmidt, 2017; Richter et al., 2017; Tilmes et al., 2017). The impact of SAI on ozone will depend strongly on the amount, altitude, geographical distribution, and timing of sulphur injections (Visioni et al., 2017).

https://doi.org/10.5194/egusphere-2026-4654
Preprint. Discussion started: 19 August 2026

Model simulations suggest that sustained large-scale SAI under high-forcing scenarios could result in pronounced ozone depletion, particularly over polar regions, thus delaying the projected ozone layer recovery, with additional variable effects in tropical and mid-latitude regions (Tilmes et al., 2020). Moreover, variations in stratospheric ozone propagate downward into the troposphere via radiative and dynamic pathways. Ozone strongly modulates UV radiation reaching the surface, affecting photolysis rates essential for ground-level ozone formation (Bornman et al., 2015). Consequently, a delayed ozone layer recovery could potentially alter ground-level ozone concentrations, with implications for air quality (Nowack et al., 2016; Zhang et al., 2016). Stratosphere–troposphere exchange (STE), driven by processes such as tropopause folding and Brewer-Dobson circulation, further influences tropospheric ozone budgets, although its magnitude and variability remain areas of active research (Neu et al., 2014; Griffiths et al., 2020; Xia et al., 2023).

Understanding and systematically monitoring the mechanisms linking potential SAI deployments with impacts on atmospheric composition throughout the middle atmosphere, in particular in terms of the stratospheric ozone layer, is therefore critical. However, the current or planned observing systems do not have the capability to fully characterize the impacts of SAI on the ozone layer, particularly with the vertical sensitivity, spatial sampling, and simultaneous chemical and thermal information needed to resolve the underlying processes (Salawitch et al., 2025). The mission concept CAIRT (Changing-Atmosphere InfraRed Tomography), proposed as a candidate mission for the 11th Earth Explorer (EE11) programme, was designed to address the broader observational gap in the middle atmosphere, by providing continuous and high-spectral-resolution mid-infrared limb measurements to derive key trace gases and temperatures over a deep column of Earth's atmosphere (European Space Agency, 2025, Sinnhuber et. al, 2026). A key application of CAIRT was the characterisation of the stratospheric ozone layer. The purpose of this study is therefore not to provide a new attribution analysis of SAI-induced ozone changes, but to use existing published WACCM6 geoengineering simulations as a pseudo-reality test case for evaluating whether CAIRT-like observations could retain and quantify such modelled ozone signals. Although CAIRT was not selected within the EE11 programme, its observational concept uniquely illustrates the kind of capability needed to monitor ozone variability under SAI scenarios, which is investigated in details in this study, underscoring the concept's potential to advance our understanding of stratospheric processes, evaluate geoengineering impacts, and improve climate projections in an era of rapid change.

2 Data and Methods

2.1 The CAIRT mission concept

The CAIRT satellite mission was a proposed concept designed to provide unprecedented three-dimensional (3D) observations of multiple parameters to characterise atmospheric dynamics and composition from a limb geometry, with a particular focus on the middle atmosphere. Although CAIRT was ultimately not selected within ESA's EE11 programme, the underlying concept - leveraging advanced limb infrared spectral imaging and tomographic retrieval techniques - remains unique in its potential to observe processes across a broad vertical domain, from the mid-troposphere (~5 km altitude) to the lower thermosphere (~115 km), with high spatial resolution in both vertical and horizontal dimensions (European Space Agency, 2025).

The overarching scientific goal of CAIRT was "to reveal, resolve, and unravel the complex coupling between composition, circulation, and climate" by characterising temperature, trace gases, aerosols, and circulation patterns across the entire middle atmosphere. The CAIRT instrument would accomplish this through thermal infrared limb emission sounding across an extended spectral range, at relatively high spectral resolution, providing vertically and horizontally resolved measurements with near-global coverage. The instrument's vertical instantaneous field of view was required to be ≤ 1.4 km below 80 km altitude and ≤ 3 km above. Horizontally, spatial sampling was specified as ≤ 25 km across-track. This enables detailed 3D reconstructions of atmospheric composition and imprints of atmospheric gravity waves, including in challenging regions such as the UTLS (European Space Agency, 2025). The vertical coverage of CAIRT was driven by the need to observe key circulation and chemical processes throughout the middle atmosphere. To ensure consistent sampling of diurnal and seasonal variability without aliasing effects, CAIRT was projected to fly in a sun-synchronous orbit with a local time of descending node at 9:30 and a 29-day repeat cycle. This orbit is comparable to that of the European Space Agency's Envisat mission, supporting inter-comparability with legacy datasets and ensuring continuity of long-term atmospheric observations. The advantages of using a mid-infrared limb sounding technique for vertically resolved composition measurements are described in detail by Sinnhuber et al., 2026.

In terms of mission design, CAIRT was guided by a rigorous set of spectral, radiometric, and geometric requirements, summarised in the CAIRT Report for Mission Selection (European Space Agency, 2025) and further detailed in CAIRT requirement specifications. To meet its scientific objectives and support operational needs, CAIRT was designed for a mission duration of at least five years (extendable), targeting near-real-time data latency for a subset of data products to enable their timely assimilation into numerical weather prediction models. The present work extends the inherent ozone analyses to a much longer period than the period of operations initially foreseen for CAIRT, in the hypothesis of a series of such instruments proving consistent observations necessary for decadal studies. The CAIRT measurement technique was already evaluated in terms of its capability to detect and characterise small SAI injections, focusing on the injected SO2 and the short-term perturbations induced to the stratospheric aerosol layer, using performance simulations described by Sellitto et al., 2026.

2.2 Pseudo-reality model runs

To test realistic SAI scenarios and their baseline reference, we used monthly output field from the Community Earth System Model version 2 with the Whole Atmosphere Community Climate Model version 6 (CESM2(WACCM6)), as contributed to the Coupled Model Intercomparison Project Phase 6 (CMIP6) (Eyring et al., 2016). The CESM2(WACCM6) model uses a finite-volume dynamical core (Gettelman et al., 2019a) with a grid spacing of 1.25° longitude × 0.95° latitude and 70 vertical levels extending from the surface up to approximately 140 km in the lower thermosphere. The model includes a prognostic treatment of stratospheric aerosols derived from volcanic and anthropogenic sulphur emissions (Mills et al., 2017), enabling realistic simulation of aerosol-related radiative and chemical processes. The CESM2 version represents the most recent and

https://doi.org/10.5194/egusphere-2026-4654
Preprint. Discussion started: 19 August 2026

comprehensive generation of the CESM family, incorporating advanced parameterizations of atmosphere, land, ocean, and sea ice processes (Danabasoglu et al., 2020). The atmospheric component can be configured in both "high-top" and "low-top" modes. In this study, the high-top WACCM6 configuration is used. This version was applied to the CMIP6 Diagnostic, Evaluation and Characterization of Klima (DECK) simulations and historical experiments, which reproduce observed surface temperature trends within the expected internal variability range (Gettelman et al., 2019b). In addition, WACCM6 provides a detailed representation of troposphere–stratosphere–mesosphere–lower thermosphere (TSMLT) chemistry, including 231 chemical species, 150 photolysis reactions, 403 gas-phase reactions, and 30 heterogeneous reactions (Emmons et al., 2020). The model has demonstrated skill in capturing the climatology of middle-atmosphere temperatures, winds, and trace species such as water vapour and ozone. It realistically reproduces key stratospheric processes, including sudden stratospheric warmings (SSWs), the quasi-biennial oscillation (QBO), the response to volcanic eruptions, and long-term ozone trends (Franke et al., 2021; Liang et al., 2022).

The simulations analysed here are based on the SSP5-3.4-OS framework and the corresponding Geoengineering SSP5-3.4-OS 2.0 experiment described by Tilmes et al. (2020). The SSP5-3.4-OS pathway is an overshoot scenario: it follows a fossil-fuel-intensive development pathway initially but later assumes reductions in fossil-fuel use and associated emissions, together with large-scale carbon dioxide removal, so that radiative forcing and mean global temperature overshoot before returning toward lower levels by 2100 (O'Neill et al., 2016). In the present study, only the period 2033–2062 is analysed, starting from the first SO_2 injection in the geoengineering simulation. Two parent scenarios simulations are used. The first is a no-SAI baseline (later on just referred to as "Baseline"). Because the SSP5-3.4-OS no-SAI simulation branches from SSP5-8.5 around 2040, the Baseline is constructed from two available no-SAI WACCM6 branches: SSP5-8.5 is used for 2033–2039, and SSP5-3.4-OS is used from 2040 onward. This provides a continuous no-SAI reference trajectory over the full 2033–2062 analysis period. The second is the Geoengineering SSP5-3.4-OS 2.0 simulation (later on just referred to as "Geoengineering"), which is used as the SAI scenario over the same period. In this simulation, stratospheric SO_2 injections are applied relative to the SSP5-3.4-OS baseline pathway, with the objective of limiting global mean warming to 2°C above pre-industrial levels while also constraining strong inter-hemispheric and pole-to-equator temperature gradients (see details on Tilmes et al., 2020). The SO_2 is injected at four predefined latitudes, 30°N, 15°N, 15°S, and 30°S, and the injection rates are adjusted annually by a feedback algorithm from January 2034 onward. The injection rates increase from the start of injection in 2034 and reach their maximum around 2050, before decreasing afterwards to intermediate values. This temporal evolution of the imposed aerosol loading is important for interpreting the pre- and post-2050 ozone trends analysed. All simulations used in this study were produced as part of the CMIP6 experiments described by Tilmes et al. (2020) and are available from the NCAR RDA archive at https://rda.ucar.edu/datasets/d651024/.

In this study, the term pseudo-reality (PR) is used for two scenarios after projection onto the CAIRT retrieval grid. For each scenario and each monthly time step, the three-dimensional ozone field is interpolated from the model grid onto the CAIRT retrieval grid using the model geopotential height field. Temperature and pressure fields are added on the same grid for estimating ozone density from mass mixing ratio. The CAIRT retrieval grid denotes the regular three-dimensional grid used

https://doi.org/10.5194/egusphere-2026-4654
Preprint. Discussion started: 19 August 2026

to represent the tomographic Level-2 atmospheric profiles along the simulated CAIRT limb-observation geometry. It is distinct from the tangent-point measurement grid. In the present retrieval simulations, the grid has an along-track sampling of approximately 50 km and consists of four across-track slices, each representing a 100 km across-track bin, with the centres of adjacent slices separated by 100 km. Here, a propagated CAIRT retrieval grid corresponding to one nominal day of orbital sampling is used.

2.3 Characterization of ozone limb-measurements under enhanced aerosol conditions

For the characterization of the CAIRT retrievals, vertical and horizontal resolution as well as retrieval uncertainties were estimated using the Linear Performance Estimator (LPE), which is described in detail by Funke et al. (2026). The LPE quantifies the retrieval response of the instrument by applying linear retrieval theory (Rodgers, 2000; von Clarmann et al., 2020) to tomographic two-dimensional limb-sounding retrievals for a range of atmospheric conditions. These conditions are selected to represent, for example, the seasonal, diurnal, and geographical variability expected during the CAIRT mission (Errera et al., 2026).

In addition to the low-stratospheric-aerosol conditions presented by Funke et al. (2026), the present study evaluates the performance of CAIRT for a case representative of the maximum global aerosol loading in the SAI scenario considered here. In 2050 the maximum injection rate of about 10 Tg SO_2/yr was applied leading to a global stratospheric aerosol load of about 23 Tg. Maximum aerosol volume densities reached approximately 4 $\mu m^3/cm^3$ (around 7 $\mu g/m^3$) in that year (compared to a typical background stratospheric aerosol load of a few tenths of $\mu m^3/cm^3$, see e.g. Günther et al. (2018)). This leads to typical limb-path optical depths of about 0.2-0.4 at the wavelengths used for ozone retrievals in the CAIRT spectral range, i.e. at around 10–12 µm. Thus, for the present SAI scenario, mid-infrared limb observations remain feasible, with aerosol transmissions on the order of 70–80%. Moreover, because the single-scattering albedo in this spectral region is only about 1% for the typical particle radii of approximately 0.4 µm occurring in the SAI scenario, the aerosol particles act predominantly as absorbers and scattering effects can safely be neglected (Höpfner, 2004; Höpfner and Emde, 2005). Thus, the aerosol contribution to the measured radiances can be accounted for in the trace-gas retrieval by co-retrieving a continuum-like absorption coefficient in addition to the target species ozone.

The resulting effects on the estimated ozone retrieval diagnostics are shown in Fig.1. Owing to the reduced limb-path transmission and the associated reduction in measurement sensitivity, the main impact is found in the spatial-resolution diagnostics, whereas the estimated retrieval uncertainties are not substantially affected. This behaviour is a consequence of the applied first-order Tikhonov regularization (Funke et al., 2026), for which the regularization strength was kept unchanged. The application of these LPE-derived diagnostic datasets to the model fields is discussed in the following section.

https://doi.org/10.5194/egusphere-2026-4654
Preprint. Discussion started: 19 August 2026

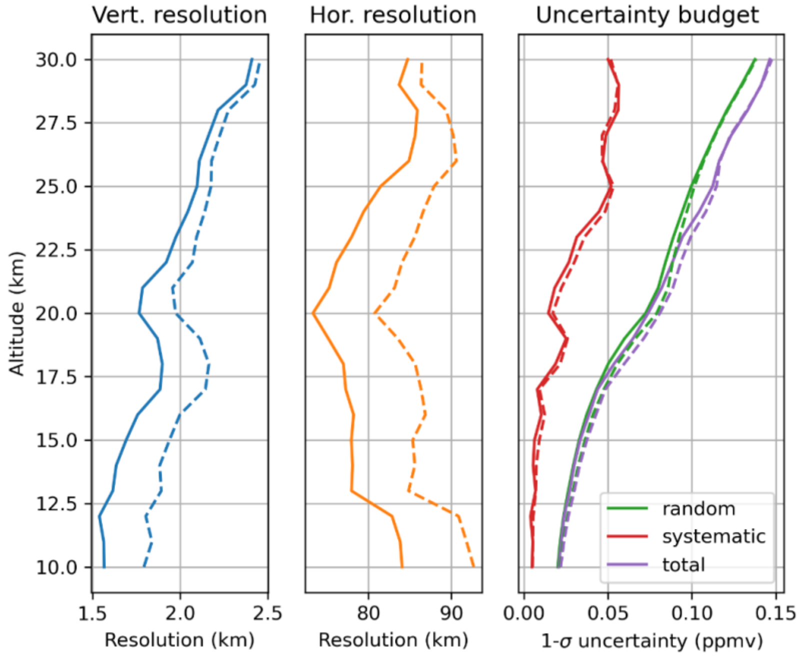

Figure 1: Diagnostics of CAIRT ozone retrievals. Left: vertical resolution; middle: horizontal resolution; right: random, systematic, and total retrieval uncertainty. Solid lines denote retrieval conditions with low stratospheric aerosol loading, while dashed lines indicate the enhanced aerosol loading associated with the investigated SAI scenario.

2.4 Description of the experiment

In this study, we assess the capability of CAIRT and CAIRT-like limb-sounding observations to detect and characterise the impacts of SAI on the stratospheric ozone layer. Because the analysis period extends over 30 years, longer than the nominal lifetime of a single CAIRT mission, the experiment should be interpreted as an assessment of a long-term CAIRT-like observing concept, or a possible series of CAIRT-like limb-sounding instruments, rather than the assessment of the performances of one single satellite mission operating continuously from 2033 to 2062. The analysis period begins with the onset of SO_2 injection and allows us to examine both the early ozone response following SAI deployment and the longer-term evolution of the ozone perturbation, including the potential delay in Antarctic ozone-hole recovery.

Figures 2a-b show global maps of the Total Ozone Column (TOC) averaged over the period 2033-2062 for the baseline (Fig. 2a) and geoengineering (Fig. 2b) PR scenarios, as well as their difference (Fig. 2c). A clear average ozone depletion due to SAI deployment, originating from the stratosphere (vertical profiles not shown here), especially at latitudes between about 30 and 90°S, is visible in Fig. 2a-c. A smaller depletion effect at northern-hemispheric high latitudes is also visible, as well as different values at other latitude ranges, including an ozone increase in the northern-hemispheric tropics and parts of mid latitudes. Differences between the two scenarios do not exceed 24 DU, i.e. 5 % of the typical values of total column ozone for the baseline. While this still is a large effect for their impacts on the environment and climate system, its characterisation with satellite observations is not obvious.

https://doi.org/10.5194/egusphere-2026-4654
Preprint. Discussion started: 19 August 2026

The two scenarios PR are used as input to the Fast L2 Simulator (FL2S, Funke et al., 2026) and the output of this step is the CAIRT pseudo-observation product, hereafter referred to as PO. It is noted that the baseline PO fields are generated using the low aerosol load LPE diagnostics, whereas the geoengineering PO are generated using the high aerosol load LPE diagnostics representative of enhanced SAI aerosol loading. Because the aerosol load evolves over the geoengineering simulation, we also use the difference between otherwise identical geoengineering PO calculations performed with the high aerosol and low aerosol LPE diagnostics as an upper-limit estimate of the additional retrieval-related error introduced by changes in aerosol loading. This estimate is relevant both for possible offsets in the geoengineering PO column, especially near the beginning of the time series, and for additional uncertainty in inferred PO trends. The parent model fields used in this study are monthly means, whereas FL2S simulates one day of CAIRT-like observations along the retrieval-grid segment. Therefore, for each monthly model state, the same monthly CAIRT-grid PR field is used as atmospheric input for 30 FL2S realisations on the same one-day retrieval-grid geometry. These realisations differ only in their random-error realisations, while the underlying atmospheric state remains fixed. The 30 FL2S outputs are then averaged to obtain one monthly mean CAIRT PO product. This approach is designed to represent the CAIRT-like retrieval response to a monthly mean atmospheric state, including smoothing, random noise, and systematic uncertainty. Random-error contributions are intrinsically reduced by averaging the 30 realisations, whereas systematic components may remain, visible as small PO–PR offsets. However, because the same monthly mean atmosphere and the same one-day orbital geometry are reused within each month, the experiment does not quantify sub-monthly atmospheric variability, day-to-day ozone variability, or the full sampling uncertainty associated with a real month of evolving orbital coverage. The results should therefore be interpreted as a monthly-mean observing-system simulation. Total and partial ozone columns are calculated by vertical integration of ozone profiles for both PR and PO products. Scenario differences are evaluated using the same CAIRT-grid sampling for PR and PO, so that PO–PR differences mainly reflect the effect of the CAIRT-like retrieval simulation rather than differences in spatial sampling. The full processing chain used to generate the CAIRT-like PO products and derive the ozone diagnostics is summarized in Fig. 3.

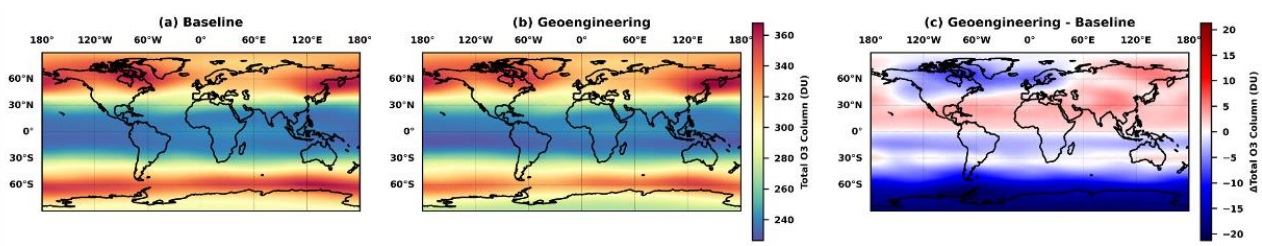

Figure 2: (a) Global maps of the total ozone column averaged derived from model over the period 2033-2062 for the baseline (see definition in the text) and (b) the geoengineering (see definition in the text) scenarios. (c) Global map of the differences of 2033-2062 total column ozone averages between the two scenarios.

https://doi.org/10.5194/egusphere-2026-4654
Preprint. Discussion started: 19 August 2026

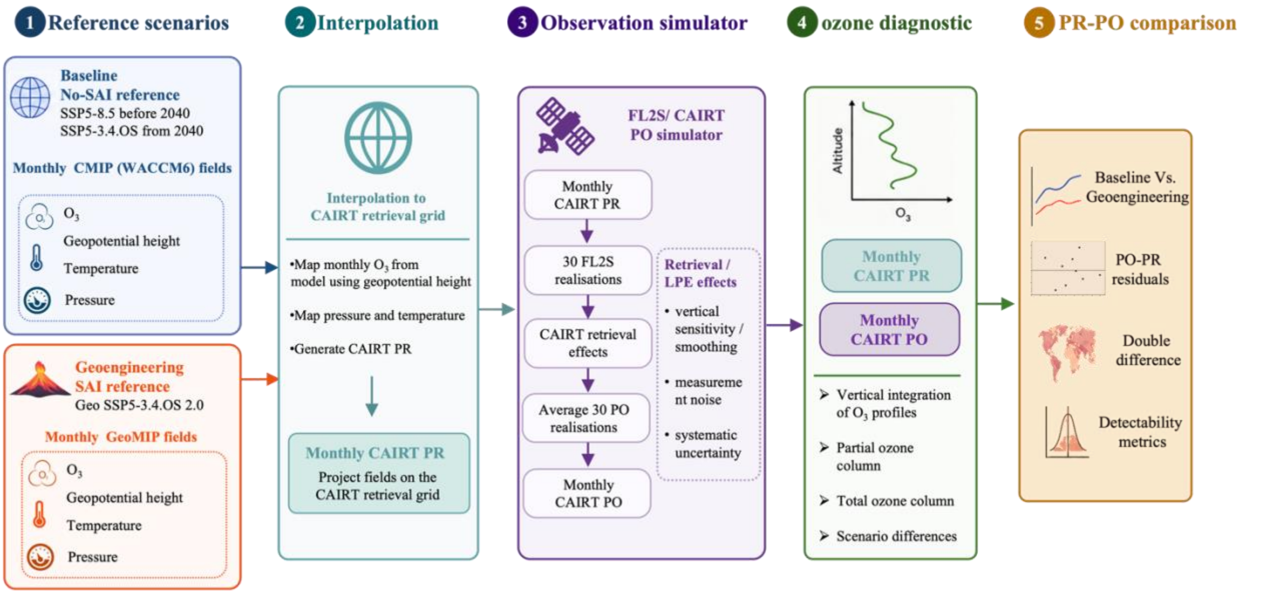

Figure 3: Scheme of the CAIRT PO simulator used in this study and subsequent analyses.

3 Results

The parent WACCM6 geoengineering simulation contains a modelled ozone response to SAI, including changes associated with enhanced stratospheric sulphate aerosol loading and related chemical and dynamical effects (Tilmes et al., 2022). Here, we use this response as the PR signal to test whether CAIRT-like PO preserve its global, regional, and seasonal structure. Specifically, we analysed whether CAIRT-like PO products retain the modelled ozone changes over 2033–2062 at global (Sect.3.1), regional (Sect.3.2) and seasonal (Sect.3.3).

3.1 Global analysis

Figure 4 shows the zonal mean ozone concentration profiles averaged over the period 2033–2062, under both baseline and geoengineering scenarios. Figures. 4a-c show the PR for both scenarios and their difference, Figs. 4d-f the respective CAIRT POs and Figs. 4g-i the differences between PR and respective PO. More specifically, Figs. 4g and 4h compare the baseline and the geoengineering simulations (PO minus PR for both scenarios), respectively, and Figure 4i displays the difference of differences - i.e., the contrast between the geoengineering-induced ozone changes in the PO scenario and that in the PR scenario. Note that a different colormap interval is used in Fig. 4i with respect to Figs. 4c-f and 4g-h.

https://doi.org/10.5194/egusphere-2026-4654
Preprint. Discussion started: 19 August 2026

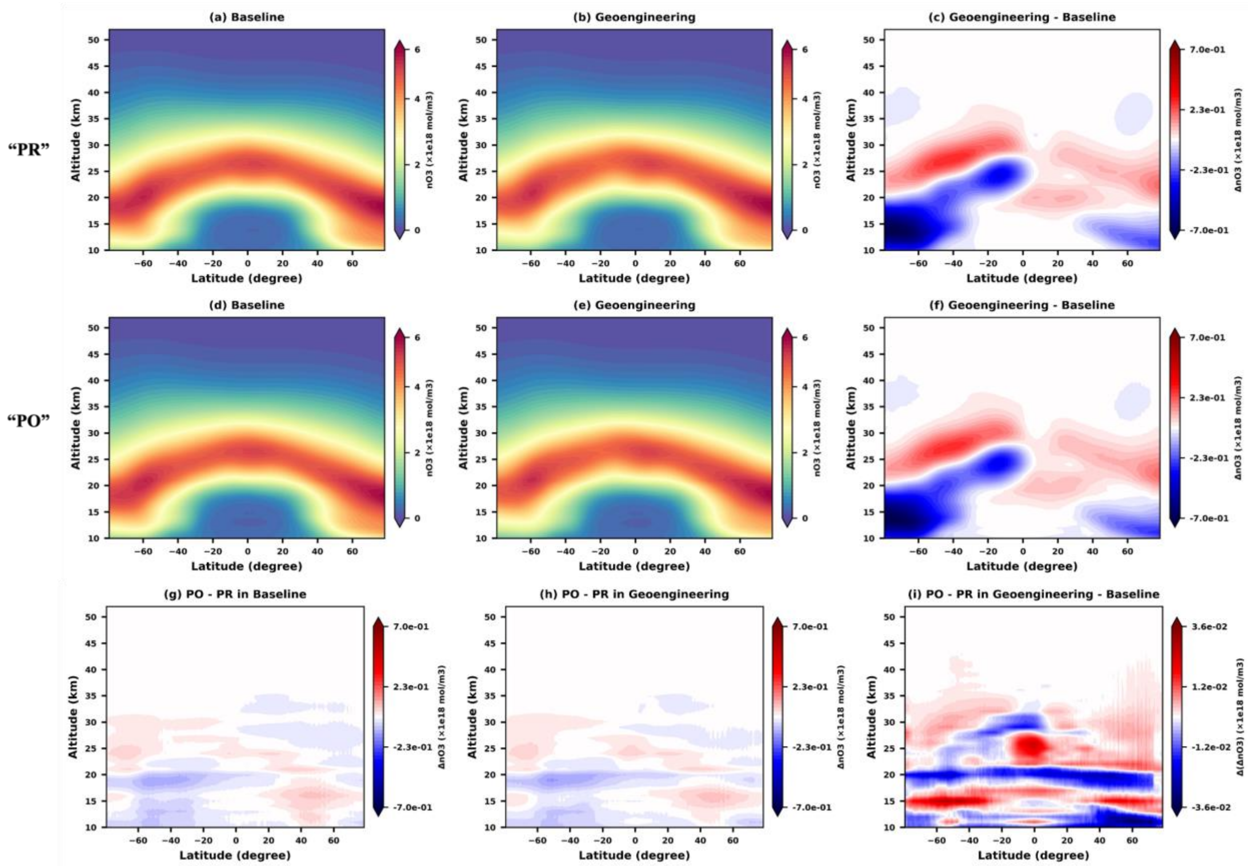

Figure 4: (a-b) Zonal mean ozone concentration averaged over 2033-2062 for the baseline and the geoengineering PR scenarios. (c) Difference in zonal mean ozone concentration between the geoengineering and the baseline PR scenarios of panels a and b. (d-f) Same as panels a-c but for the CAIRT PO. (g-h) Differences between PO and PR for the baseline (panel g) and the geoengineering scenario (panel h). (i) Zonal mean of the double differences, i.e., (geoengineering – baseline) PO – (geoengineering – baseline) PR, note the different scale compared to panels c and f.

The PRs show a marked reduction in ozone concentrations after the SAI intervention, between about 10 and 20 km, and an increase between about 20 and 30 km, at high latitudes in both hemispheres, with a much larger impact in the high-latitudes Southern Hemisphere. This is a well-known effect of the combination of sulphate-aerosols-enhanced heterogeneous chemistry, changes in temperature, and transport, as mentioned by Tilmes et al. (2022) for SAI deployments, and not unlike the effect of large volcanic eruptions. The SAI-induced ozone depletion reaches higher altitudes in the southern-hemispheric tropics, following the latitude variability of the tropopause altitude, accompanied by an ozone increase in the northern-hemispheric tropics. A visual comparison between the differences of the two scenarios for PR and PO reveals that both PR and PO exhibit very similar pattern of the zonal mean ozone fields and the preceding vertical and zonal patterns, over the three-decade period (compare Figs. 4c and f). Quantitatively, PR scenarios are characterised by a spatial-temporal mean SAI-induced ozone decrease of -1.13 %, with local variations ranging between -22 % and +9 %, between the baseline and the geoengineering scenarios. Similarly, the CAIRT PO indicates an average decrease of –1.08 %, with variations between -21 % and +8 %. The

https://doi.org/10.5194/egusphere-2026-4654
Preprint. Discussion started: 19 August 2026

differences between CAIRT PO and the PR, for the two scenarios, are extremely small with the mean bias of about $+0.5 \times 10^{15}$ mol m⁻³ and root mean square error of 7×10^{15} mol m⁻³. Each PR scenario differs much less from their respective CAIRT PO than one PR scenario with respect to the other, or one PO dataset with respect to the other (compare Figs. 4g and h with Figs. 4c and f). These quantitative analyses demonstrate that the CAIRT PO can describe the two different PR scenarios (with or without SAI interventions) and distinguish between the two. The synthetic CAIRT-derived ozone products can preserve the modelled SAI-induced long-term ozone signal with only small retrieval-induced deviations, thereby suggesting that a series of CAIRT-like instruments could provide an observing system for monitoring global ozone variability and assessing global geoengineering impacts at the decadal time scale.

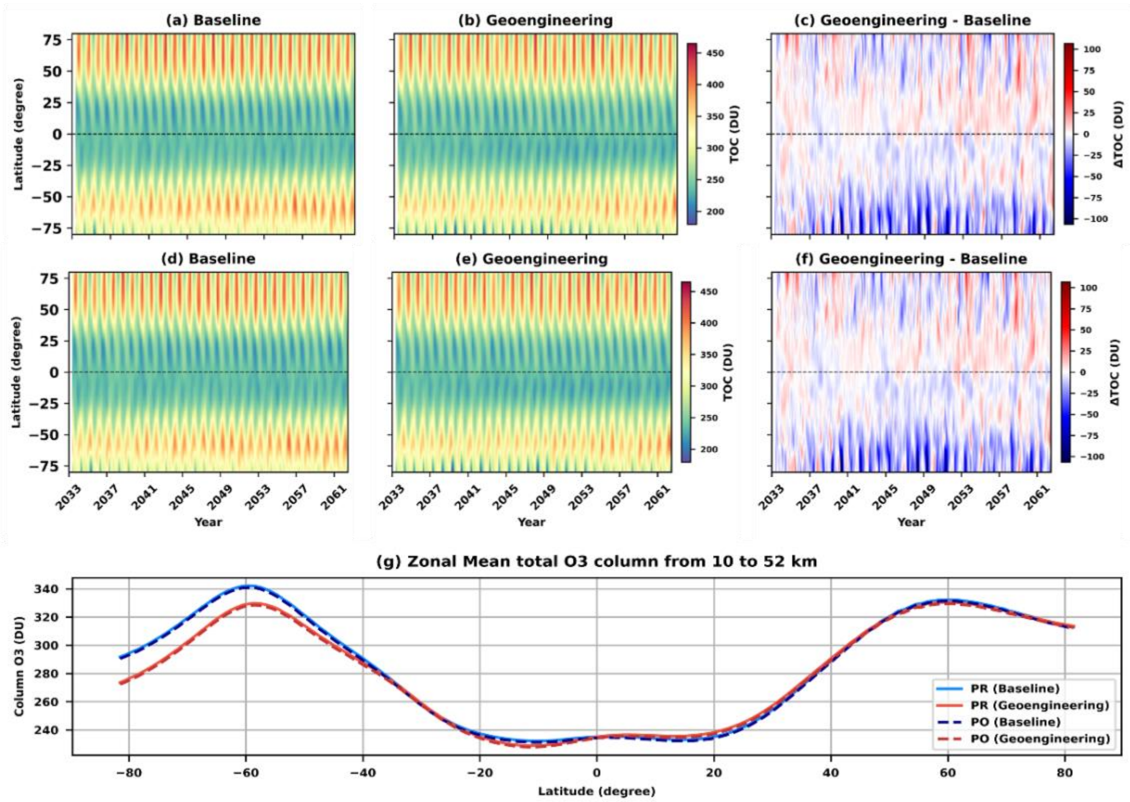

Figure 5: Latitude–time evolution of zonal-mean total ozone column over 2033–2062. Panels (a–c) show the PR fields for the baseline and geoengineering scenarios and their difference, while panels (d–f) show the corresponding CAIRT POs. Panel (g) shows the 2033–2062 mean zonal total ozone column, obtained by averaging over longitude and time at each latitude.

After discussing the observability of ozone concentration profile changes due to SAI, we analyse the spatiotemporal variability of the total ozone column fields. Total ozone column is estimated here as the vertical integral of ozone number density between 10 and 52 km. Lower altitudes are not impacted by this SAI scenario. Figure 4 presents the latitude–time evolution of zonal-mean total ozone column over the period 2033–2062 for both the PR simulations and the corresponding CAIRT POs. As for Fig. 4, Fig. 5 shows the PR fields for the baseline and geoengineering scenarios and their difference (first row), and the

https://doi.org/10.5194/egusphere-2026-4654
Preprint. Discussion started: 19 August 2026

corresponding CAIRT PO fields (second row). Figure 5g shows the 2033–2062 mean zonal total ozone column variability, obtained by averaging the total ozone column over longitude and time at each latitude, for both PR and PO in the baseline and geoengineering scenarios. The CAIRT PO can clearly differentiate between the two scenarios in the high-latitudes Southern Hemisphere, while marked measurable differences, in this zonal average, cannot be clearly distinguished in the Northern Hemisphere.

The geoengineering–baseline difference in the PR fields represents the modelled SAI-induced ozone response. The purpose of the CAIRT PO comparison is therefore to test whether this modelled (pseudo-real) response is observable and captured accurately with such kind of concept observing system. Over the full latitude–time domain, the PR simulations show a mean geoengineering–baseline total ozone column difference of −3.0 DU and with a standard deviation of 12.3 DU. The corresponding CAIRT POs give a very similar mean difference of −3.1 DU and with a standard deviation of 12.3 DU. As highlighted before, the strongest coherent negative response occurs at southern high latitudes. Over 30–82°S, the mean geoengineering–baseline difference is −9.9 DU in the PRs and −9.7 DU in the POs, with the 5th percentile reaching approximately −40 DU in both cases. This signal is, thus, clearly distinguished by CAIRT-like instruments. The Northern Hemisphere zonal-mean response is weaker and less coherent over the analysed period. In general, the CAIRT PO fields closely reproduce the corresponding PR latitude–time structures. This is especially clear in the long-term zonal-mean profiles, where the PR and PO curves nearly overlap for both scenarios. Quantitatively, the PO–PR biases are much smaller than the geoengineering–baseline scenario signal on the ozone layer. For the baseline case, the PO–PR bias has a mean value of −1.02 DU with a root mean square error of 0.16 DU. For the geoengineering case, the corresponding mean bias and root mean square error are −1.18 DU and 0.17 DU, respectively. Thus, the CAIRT PO simulator introduces a small systematic column offset, but this offset is similar in both scenarios.

To evaluate whether the CAIRT PO modifies the PR scenario difference itself, we calculated the double difference as $D = (TOC_{geo,PO} - TOC_{base,PO}) - (TOC_{geo,PR} - TOC_{base,PR})$, with TOC the total ozone column from 10 to 52 km. This double difference has a mean value of −0.16 DU with a standard deviation of 0.08 DU over the 2033–2062 latitude–time domain. This corresponds to only 1.4 % of the difference of the PR geoengineering–baseline signal. The correlation between the PR and PO scenario-difference fields is 0.99997, indicating that the CAIRT PO processing preserves both the amplitude and the latitude–time structure of the modelled SAI-induced total ozone column response. Over 30–82°S, where the strongest ozone response occurs, the double-difference is even smaller, with means about -0.14 DU and 0.04 DU as a standard deviation.

Figure 6 supports the evaluation of the sensitivity of the geoengineering PO product to the choice of LPE diagnostics under enhanced aerosol loading. For this purpose, we compare otherwise identical geoengineering PO calculations generated with the low aerosol and high aerosol LPE diagnostics as shown in Fig. 1. The difference between these two PO products is used as an upper-limit estimate of the additional retrieval-related error caused by changes in aerosol loading during the geoengineering simulation. For total ozone column, this difference has a mean value of −0.16 DU, a standard deviation of 0.08 DU with values ranging from −0.39 to +0.09 DU. These values are very small compared with the global and southern high-latitude geoengineering–baseline signals discussed above, indicating that the use of the enhanced-aerosol LPE diagnostics does

https://doi.org/10.5194/egusphere-2026-4654
Preprint. Discussion started: 19 August 2026

not substantially affect the inferred large-scale SAI ozone response. This also indicates that a CAIRT-like instrument would be able to observe stratospheric ozone without losing accuracy, also in conditions of large stratospheric aerosol burdens typical of full-blown SAI deployments or, incidentally, of large volcanic eruptions (Pinatubo-sized).

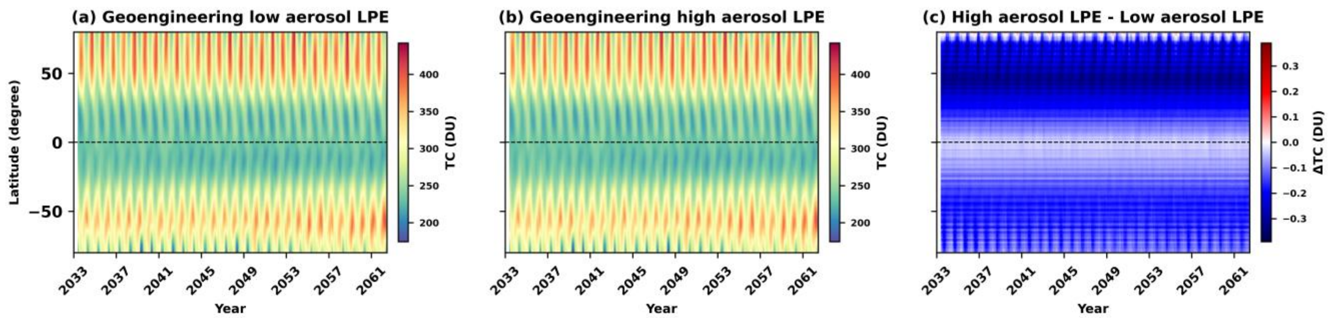

Figure 6: Latitude–time evolution of zonal-mean total ozone column over 2033–2062. Panels (a-c) shows geoengineering PO fields for the low and high aerosol LPE and their difference.

Overall, Figures 5 and 6 shows that the CAIRT PO product does not artificially create or suppress the modelled SAI signal. Instead, it preserves the large-scale geoengineering–baseline response with only small pseudo-observations-induced residuals. This comparison is therefore to be interpreted as a consistent test of the CAIRT-like pseudo-observation performances in quantitatively characterising the long-term global impact of the SAI effects on the stratospheric ozone layer, for this specific SAI scenario.

3.2 Regional analysis

In this section, we analyse the capability of CAIRT-like instruments to characterise the impacts of SAI interventions on the ozone layer in the identified regions of specific interest for these impacts, i.e. high-latitudes regions. This analysis is based on regional-mean total ozone column integrated between 10 and 52 km over the Antarctic high-latitude band, 60–82°S, and the Arctic high-latitude band, 60–82°N. The purpose of this regional analysis is to test whether the regional geoengineering–baseline signal present in the PR simulations is retained in the CAIRT POs.

In the Antarctic region, the time series of total ozone column over 60–82°S for the PR and CAIRT PO and the two scenarios is shown in Fig. 7. The curves show monthly regional means smoothed with a 1-year running mean for clearer visualization, while the quantitative statistics below are calculated from the annual means (without temporal smoothing). The geoengineering–baseline difference represents the modelled SAI-induced Antarctic ozone response in the PR simulations; the role of the CAIRT PO comparison is to test whether this regional signal is retained in the pseudo-observed fields. In the PR simulations, the geoengineering case has lower ozone columns than the baseline by a mean of −16.54 DU, corresponding to −5.18 %, with an interannual variability of 9.74 DU and anomalies ranging from −33.71 to +3.46 DU. The CAIRT POs give an almost identical regional signal, with a mean geoengineering–baseline difference of −16.67 DU (−5.24 %), the same interannual variability of 9.74 DU, and anomalies ranging from −33.83 to +3.34 DU. Both scenarios show a positive total

https://doi.org/10.5194/egusphere-2026-4654
Preprint. Discussion started: 19 August 2026

ozone column trend when the full 2033–2062 period is considered, but this full-period trend masks an important difference in the timing of Antarctic ozone recovery. In the baseline PR fields, ozone recovery is already evident before 2050, with a significant trend of +10.80 DU decade^{-1}, and remains positive after 2050, with +10.50 DU decade^{-1}. In contrast, the geoengineering PR fields show no recovery before 2050, with a trend of −2.75 DU decade^{-1}. A clear recovery signal only appears from 2050 onward, when the trend becomes strongly positive, +15.71 DU decade^{-1}. The CAIRT-like PO trends capture both the lack of a significant pre-2050 recovery under geoengineering of −2.76 DU decade^{-1} and the strong post-2050 recovery of +15.70 DU decade^{-1}. It is noted that trends in total ozone column are calculated using ordinary least-squares linear regression. For the all-month regional analyses, monthly regional-mean total ozone columns are first averaged to annual means, and the regression is then applied to the annual time series. The results indicates that the CAIRT POs are able not only to retrieve the long-term trend, but also to distinguish between periods with and without a detectable recovery signal. This indicates that the modelled Antarctic ozone recovery is faster under SAI than in the no-SAI baseline after 2050, with the CAIRT POs catching this difference.

In addition to these analyses, we also calculated the biases and root mean square errors of PO versus PR for both scenarios to test the accuracy of the pseudo-observed fields with respect to PR. The PO–PR bias is −1.21 DU for the baseline and −1.34 DU for the geoengineering case, this offset being nearly scenario independent. As a result, the bias in the geoengineering–baseline signal itself is only −0.13 DU, with Root Mean Square Error (RMSE) of 0.13 DU between the PR and PO signals. Thus, the CAIRT PO product preserves the modelled Antarctic SAI-induced total ozone column anomaly while introducing only a very small residual in the scenario difference.

To further examine the Antarctic spring response, we present October total ozone column over 60–82°S separately in Fig. 8. This is the month during which the largest ozone hole impacts occur (Crutzen and Arnold, 1986). In the PR fields, the geoengineering case is lower than the baseline by −23.80 DU (−7.56 %), larger when compared with −16.54 DU (−5.18 %) for the all-month annual-mean analysis mentioned above. The corresponding CAIRT PO difference is almost identical, −23.91 DU (−7.63 %). The bias in the geoengineering–baseline signal introduced by the PO with respect to PR is −0.11 DU with RMSE of 0.11 DU, indicating that the CAIRT POs preserve the modelled Antarctic spring ozone anomaly with negligible perturbation. The October trends further highlight the delayed recovery under geoengineering. Over the full 2033–2062 period, both scenarios show positive PR trends, with +19.56 DU decade^{-1} for the baseline and +18.80 DU decade^{-1} for the geoengineering case. However, splitting the period before and after 2050 reveals a clearer difference. In the baseline, October ozone increases both before and after 2050, with trends of +24.40 and +24.55 DU decade^{-1}, respectively. In contrast, the geoengineering case shows no recovery before 2050, with a negative trend of −7.14 DU decade^{-1}, followed by a strong positive trend after 2050 of +30.03 DU decade^{-1}. The CAIRT POs reproduce these trends as: +19.56, +24.41, and +24.56 DU decade^{-1} for the baseline full, pre-2050, and post-2050 periods, and +18.79, −7.16, and +30.04 DU decade^{-1} for the corresponding geoengineering periods. Thus, for October as well as for the annual Antarctic mean, the POs capture both the absence of an early recovery signal under geoengineering and the emergence of a strong recovery in the 2050s.

https://doi.org/10.5194/egusphere-2026-4654
Preprint. Discussion started: 19 August 2026

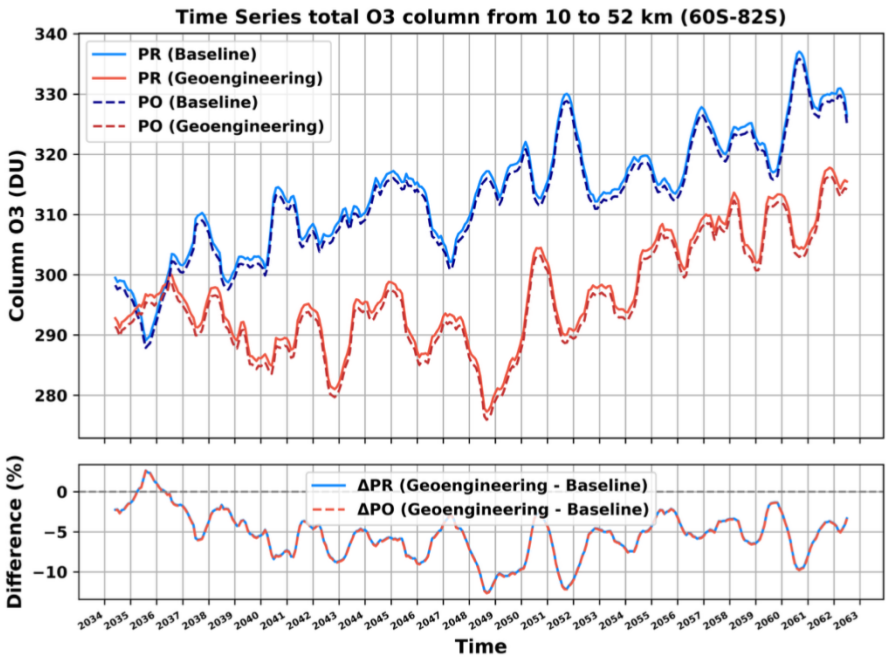

Figure 7: **Regional-mean total ozone column integrated between 10 and 52 km over 60–82°S, monthly time series from 2033 to 2062. The upper panel shows the baseline and geoengineering PR simulations and the corresponding CAIRT PO products. The lower panel shows the relative geoengineering–baseline difference for PR and PO. A 12-month running mean is shown for visualization.**

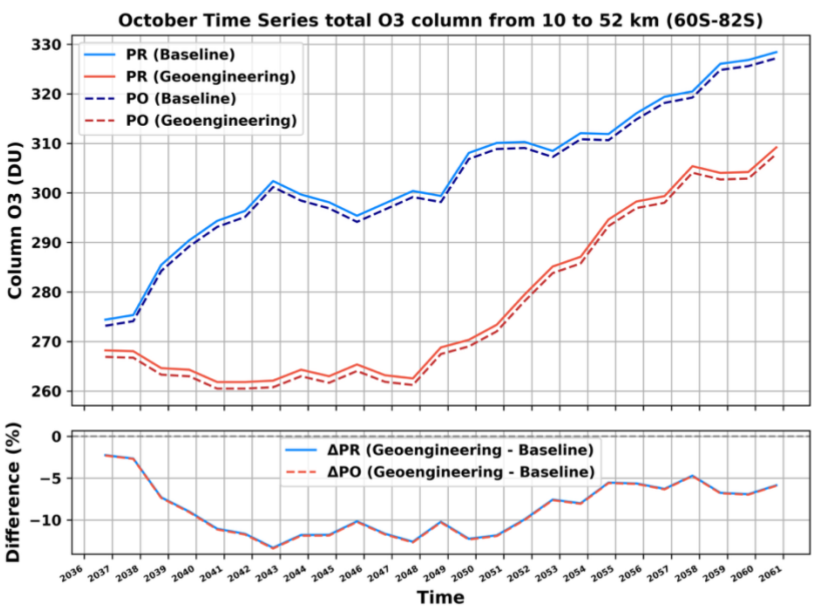

Figure 8: Same as Fig. 7 but only with October regional means. A 5-year running mean is shown for visualization.

The corresponding Arctic (60–82°N) regional analysis is shown in Fig. 9. Visually, the SAI impact, for this scenario, is not as strong as in the Antarctic region and indeed hardly discernible. In the PR fields, the geoengineering case is lower than the

https://doi.org/10.5194/egusphere-2026-4654
Preprint. Discussion started: 19 August 2026

baseline by only −0.74 DU (−0.23 %), with an interannual variability of 6.54 DU and anomalies ranging from −10.43 to +13.13 DU. The corresponding CAIRT PO signal is very similar, −0.93 DU (−0.29 %), with almost identical variability and anomaly range. The Arctic trends are also weaker and less distinct than in the Antarctic region. In the PR fields, the baseline trend is +3.32 DU decade^{-1}, while the geoengineering trend is +2.51 DU decade^{-1}. The corresponding PO trends are nearly identical, +3.33 DU decade^{-1} and +2.51 DU decade^{-1}, respectively. Because the geoengineering–baseline difference is small compared with interannual variability and the trend confidence intervals overlap, this Arctic regional diagnostic does not provide evidence for a robust SAI-induced total ozone column reduction over 60–82°N. The PO–PR agreement remains strong: the bias in the geoengineering–baseline signal is only −0.19 DU, with RMSE = 0.19 DU, indicating that the CAIRT POs does not introduce an artificial SAI-ozone signal in this region.

March is analysed separately as an Arctic late-winter/spring ozone diagnostic (Bednarz et al., 2016), and the time series is presented in Fig. 10. The result remains consistent with the all-month regional analysis. In the PR fields, the March geoengineering–baseline difference is −0.73 DU (−0.19 %), while the corresponding CAIRT PO difference is −0.91 DU (−0.23 %). These differences are small compared with the March interannual variability of about 10.51 DU, and the anomaly range changes sign from year to year (−24.19 to +28.35 DU in PR). The PO-induced residual in the March scenario difference is again very small, with a signal bias of −0.18 DU, RMSE = 0.19 DU. Thus, for this model experiment, CAIRT PO preserves the weak Arctic PR response but does not turn it into a robust detectable signal.

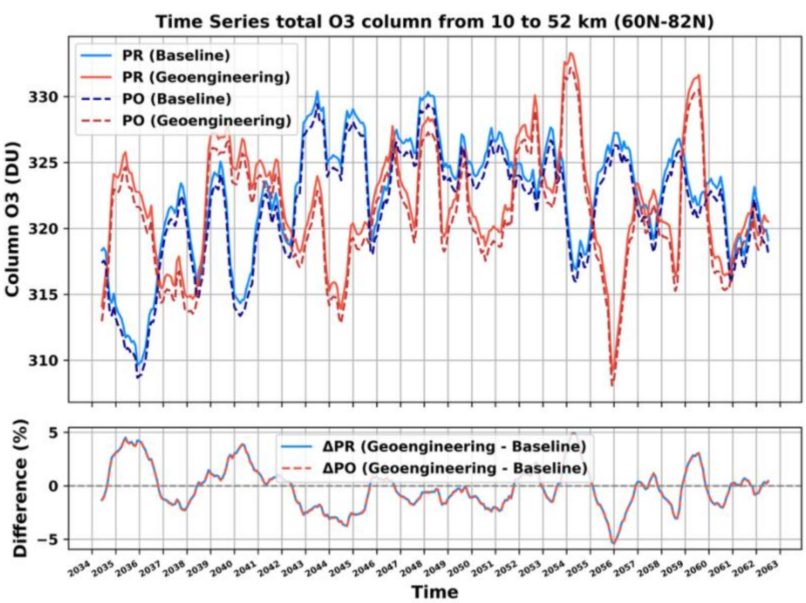

Figure 9: Regional-mean total ozone column integrated between 10 and 52 km over 60–82°N, monthly time series from 2033 to 2062. The upper panel shows the baseline and geoengineering PR simulations and the corresponding CAIRT PO products. The lower panel shows the relative geoengineering–baseline difference for PR and PO. A 12-month running mean is shown for visualization.

https://doi.org/10.5194/egusphere-2026-4654
Preprint. Discussion started: 19 August 2026

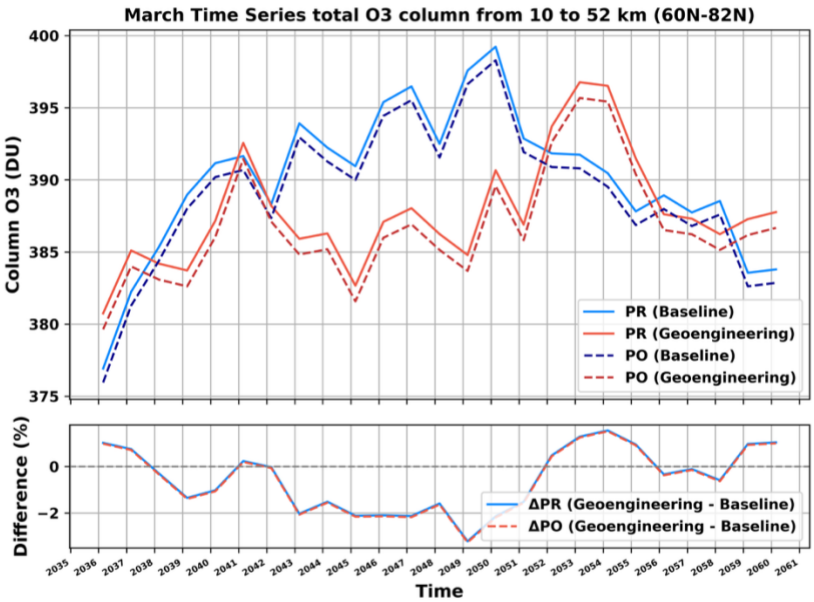

Figure 10: Same as Fig. 9 but only with March regional means. A 5-year running mean is shown for visualization.

In the Arctic, the recovery signal is less robust than in Antarctica. The baseline PR fields show a weak positive trend over the full period, +3.32 DU decade^{-1}, mainly driven by a significant increase before 2050, +12.54 DU decade^{-1}. After 2050, however, the baseline trend becomes negative −3.90 DU decade^{-1}. Under geoengineering, the full-period Arctic trend is not statistically significant +2.51 DU decade^{-1}, and the post-2050 trend also remains non-significant −1.46 DU decade^{-1}. As for Antarctica, the PO trends follow the PR trends, indicating that when the recovery signal is weak or absent, the pseudo-observations do not introduce an artificial trend.

The sensitivity of the regional trend analysis to temporally changing aerosol-dependent retrieval conditions was estimated by scaling the mean difference between the high-aerosol and low-aerosol geoengineering PO products with the annual SO_2 injection-rate trajectory. The resulting time-dependent retrieval offsets were fitted over the same pre- and post-2050 periods used for the ozone trend analysis. Before 2050, the estimated retrieval-related trend contributions are -0.082 DU decade^{-1} for the Antarctic annual mean and -0.065 DU decade^{-1} for October. After 2050, the corresponding contributions are +0.033 and +0.026 DU decade^{-1}, respectively. In the Arctic, the corresponding pre-2050 estimates are -0.11 DU decade^{-1} for the annual mean and -0.10 DU decade^{-1} for March, while the post-2050 estimates are +0.044 and +0.041 DU decade^{-1}, respectively. The Arctic values should be regarded as upper-limit estimates because the high-aerosol LPE diagnostics represent stronger aerosol conditions than those occurring at northern high latitudes. Across all regions and seasons considered, these aerosol-related trend errors amount to at most about 6% of the corresponding 95% confidence-interval half-widths and therefore do not affect the conclusions of the regional trend analysis. This calculation provides an order-of-magnitude estimate because it assumes that the retrieval offset scales with the SO_2 injection rate, which is used here as a proxy for aerosol loading.

https://doi.org/10.5194/egusphere-2026-4654
Preprint. Discussion started: 19 August 2026

To facilitate direct comparison across regions, Table 1 summarises the key diagnostics (mean values, differences, variability, and trends) for the Northern Hemisphere high latitude (60–82° N), Northern Hemisphere mid and low-latitudes (0–60° N), Southern Hemisphere mid and low-latitudes (0–60° S) and Southern Hemisphere high latitude (60–82° S). The metrics include baseline and geoengineering mean total ozone column (TOC, Dobson Units), their differences (absolute and percent), interannual standard deviation (σ), and linear trends (DU dec^{-1} with 95% confidence intervals).

Table 1: Summary of total ozone column diagnostics for three key latitude bands: NH high latitude (60–82° N), NH mid and low latitude (0-60° N), SH mid and low latitude (0-60° S), and SH high latitude (60–82° S). Values are shown for both full model simulations (PR) and CAIRT-like pseudo-observations (PO) under the baseline and geoengineering (Geo SSP5-OS-34 2.0) scenarios.

Region (lat band)	Scenario	Mean TOC Baseline (DU)	Mean TOC Geo (DU)	ΔTOC (DU, %)	Interannual σ (DU)	Trend Baseline (DU/dec)	Trend Geo (DU/dec)
NH high-lat (60–82°N)	PR	323.73	322.99	-0.74 (-0.23)	6.54	3.32 [0.75, 5.89]	2.51 [0.01, 5.00]
	PO	322.79	321.86	-0.93 (-0.29)	6.54	3.33 [0.76, 5.90]	2.51 [0.02, 5.00]
NH mid&low-lat (0–60°N)	PR	262.97	264.64	1.67 (0.63)	3.15	0.96 [-0.38, 2.30]	2.18 [0.88, 3.48]
	PO	262.07	263.55	1.48 (0.56)	3.15	0.96 [-0.38, 2.29]	2.18 [0.88, 3.48]
SH mid&low-lat (0–60°S)	PR	265.10	261.96	-3.14 (-1.18)	2.61	0.16 [-0.98, 1.31]	0.21 [-0.90, 1.31]
	PO	263.99	260.75	-3.25 (-1.23)	2.61	0.16 [-0.99, 1.31]	0.20 [-0.90, 1.31]
SH high-lat (60–82°S)	PR	319.36	302.82	-16.54 (-5.18)	9.74	9.85 [7.90, 11.80]	7.91 [5.09, 10.72]
	PO	318.15	301.48	-16.67 (-5.24)	9.74	9.85 [7.89, 11.80]	7.91 [5.09, 10.72]

3.3 Seasonal Analysis

As a further analysis of CAIRT PO adequacy for characterising long-term SAI impacts on the stratospheric ozone layer, we also analyse seasonal cycles. Figure 11 shows the 30-year monthly climatology of stratospheric ozone column over 60–82°S and 60–82°N with error bars representing ±1 interannual standard deviation for each month (panels a–b) and the fitted seasonal amplitude (peak-to-trough, panel c). In the Southern Hemisphere, CAIRT PO and PR simulations have virtually identical seasonal shapes (normalized root-mean-square error, NRMSE < 4%), where NRMSE is the mean PO–PR difference normalized by the seasonal amplitude and thus quantifies shape similarity. Harmonic regression confirms this agreement and quantifies the change: in the PRs, the annual-harmonic amplitude (A1) increases from ~11.38 DU (baseline) to ~26.6 DU (geoengineering), while the seasonal amplitude — defined as the fitted peak-to-trough range — grows from ~34.4 DU to ~65.75 DU (Δ ≈ +31 DU), as an effect of the enhanced ozone depletion by SAI. The seasonal maximum changes from July (baseline) to August (geoengineering), whereas the minimum occurs later in the year, moving from March to November (here

https://doi.org/10.5194/egusphere-2026-4654
Preprint. Discussion started: 19 August 2026

this refers to a change in the timing (month) of the annual maximum or minimum). These amplitude and phase changes are captured consistently by CAIRT PO. The error bars indicate substantial interannual variability, especially during the months with the strongest Antarctic geoengineering–baseline deviations. We therefore repeated the standard-deviation calculation separately before and after 2050 to test whether this variability is mainly associated with the SAI ramp-up phase. For the CAIRT-like PO products, the mean October–December standard deviation in the geoengineering case decreases from 22.9 DU over 2033–2062 to 19.3 DU after 2050, while the corresponding post-2050 baseline value is 15.0 DU. This indicates that restricting the analysis to the post-2050 period reduces the variability, but that interannual variability remains important. The mean October–December geoengineering–baseline signal remains large, −34.6 DU over the full period and −31.8 DU after 2050. Assuming that the standard error decreases approximately as $1/\sqrt{N}$, the estimated interannual variability implies that approximately four years of observations would need to be averaged to detect the Antarctic seasonal signal at the 95% confidence level over the full period.

In contrast, over the Northern Hemisphere, PO and PR again show excellent shape agreement (NRMSE < 1 %), but SAI does not produce any appreciable change in either A1 (~69.43 DU to ~69.27 DU) or the seasonal amplitude (~140.05 DU to ~140.11 DU), and no phase shift (seasonal trends for geoengineering and baseline PR almost identical). Consequently, no individual Northern Hemisphere month meets the combined detectability criteria. Together, these results demonstrate that CAIRT-like PO products reproduce the seasonal cycle with high fidelity and can provide a robust multi-year observational diagnostic of seasonal-cycle modifications where the modelled SAI signal is sufficiently large, without spuriously indicating changes where the signal is weak or absent.

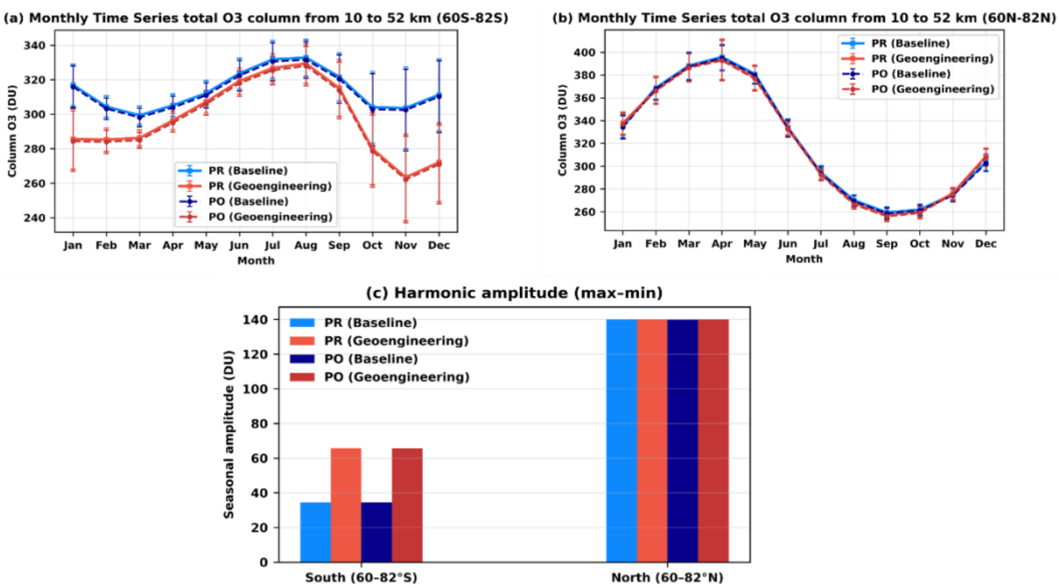

Figure 11: Seasonal cycle of total ozone column. (a–b) Thirty-year (2033–2062) monthly means over the SH and NH high latitudes, 60–82°S and 60–82°N, for the PR and PO, each shown for the baseline and geoengineering PR scenarios. Error bars indicate ±1 interannual standard deviation for each month. (c) Corresponding seasonal amplitude.

https://doi.org/10.5194/egusphere-2026-4654
Preprint. Discussion started: 19 August 2026

4 Conclusions

This study investigates the capability of a high-spectral-resolution infrared limb-emission observing concept, modelled around the technical specifications of the proposed EE11 CAIRT mission, to detect and quantitatively characterise modelled ozone responses to SAI. The analysis uses existing CESM2(WACCM6) CMIP6 scenario simulations as parent model fields and evaluates how these fields would be represented in CAIRT-like PO. The study should therefore be interpreted as an observing-system assessment, rather than as a new attribution study of SAI-induced ozone chemistry or dynamics. To do this, we use existing PR scenarios generated, in the context of the CMIP6 programme, with CESM2(WACCM6) under the SSP5-3.4-OS social development pathway framework, with ("geoengineering" scenario) and without ("baseline" scenario) SAI deployment. Synthetic CAIRT PO were generated for the two PR scenarios using a realistic CAIRT PO simulator. The parent WACCM6 PR fields used in this study show a spatially heterogeneous ozone response to SAI. A larger total ozone column reduction occurs in the southern-hemispheric high-latitudes region, while smaller negative or positive anomalies are present in some other latitude bands.

At the global latitude–time scale, the PR simulations show a mean geoengineering–baseline total ozone column from 10 to 52 km difference of −2.95 DU, while the corresponding CAIRT POs give −3.11 DU, with the same standard deviation of 12.3 DU. Over the southern high latitudes, 30–82°S, the mean SAI-induced reduction reaches −9.78 DU in the PRs and −9.92 DU in the PO. The PO processing preserves this signal with only a very small double-difference bias of −0.16 DU, corresponding to about 1.4 % of the PR geoengineering–baseline signal. These results show that the CAIRT-like PO product preserves both the amplitude and the latitude–time structure of the modelled SAI-induced total ozone column response.

The regional analysis confirms that the strongest and most robust SAI-induced ozone perturbation occurs over Antarctica. Over 60–82°S, the geoengineering case is lower than the baseline by −16.54 DU in the PR fields and by −16.67 in the CAIRT PO. The PO-induced residual in the Antarctic geoengineering–baseline signal is only −0.13 DU, demonstrating that the pseudo-observations preserve the regional SAI-induced ozone depletion with negligible distortion. In October, when Antarctic ozone-hole impacts are largest, the depletion is even stronger, reaching −23.80 DU in the PR fields and −23.91 DU in the PO. The trend analysis further shows that SAI modifies the timing of Antarctic ozone recovery. In the baseline PR fields, Antarctic total ozone column increases both before and after 2050, with trends of +10.80 and +10.80 DU decade^{-1}, respectively. In contrast, the geoengineering PR fields show no recovery before 2050, with a trend of −2.75 DU decade^{-1}, followed by a strong recovery signal after 2050 of +15.71 DU decade^{-1}. The CAIRT POs reproduce these values almost exactly, with a pre-2050 geoengineering trend of −2.76 DU decade^{-1} and a post-2050 trend of +15.70 DU decade^{-1}. Thus, the main impact of SAI in this scenario is not simply a uniformly slower recovery over the whole period, but rather a delay in Antarctic ozone recovery until the 2050s, followed by a stronger positive trend afterwards. The CAIRT concept proved also very robust in terms of ozone retrievals in large aerosol burdens.

A limitation of the present methodology is that the simulated PO data do not include long-term instrumental drift, observing-system degradation, or possible biases between consecutive payloads. Although such effects could in principle be incorporated into the LPE–FL2S framework, their quantitative pre-flight assessment is difficult. In practice, inter-payload biases would need to be minimized through cross-calibration during mission overlap phases. In addition, stability assessments against ground-based networks could help identify and correct instrumental drifts in CAIRT-like stratospheric ozone observations. Previous studies suggest that such approaches can support ozone-trend stability at the level of about 2–3 % per decade (Hubert et al., 2016), which would be important for the robust detection of statistically significant SAI-induced trends.

Despite these limitations, this study demonstrate that CAIRT-like limb-sounding observations would provide a robust capability for monitoring the large-scale and long-term ozone response to SAI in the pseudo-real scenario, especially in regions where the signal is coherent and exceeds natural variability in the PR. Across global, regional, trend, and seasonal diagnostics, the CAIRT POs closely follow the corresponding PR fields, with PO-induced residuals much smaller than the modelled SAI-induced ozone anomalies. This indicates that a series of CAIRT-like instruments would be able to quantitatively characterise coherent SAI ozone impacts where they exceed variability, while not producing artificial signals in regions where the modelled response is weak or not robust. Although CAIRT was not selected within ESA's EE11 programme, the recent selection of NASA's STRIVE mission demonstrate that similar limb-infrared observing capabilities remain a priority in the near-term satellite observing portfolio.

Competing interests

Some authors are members of the editorial board of journal AMT. The authors declare that they have no competing interests.

Author contributions

MK, PS, and MH designed the study. MK and PS developed the CAIRT PO simulator. MH, BF, JU and QE provided the elements needed to develop the CAIRT PO simulator. ST provided the modelling data for the PR scenarios. MK run the PO simulations. BMS and AH contributed to funding acquisition and administration of the global CAIRT project. MK wrote the first version of the manuscript that was reviewed by all authors.

Funding

This work has been supported by the European Space Agency through the CAIRT PerRec and the STATISTICS projects, and the Centre National d'Études Spatiales (CNES) through the EXTRA-SAT grant.

5 References

European Space Agency: Report for Mission Selection: Earth Explorer 11 Candidate Mission CAIRT , https://doi.org/10.5281/zenodo.15606819, June 2025.

Aubry, T. J., Engwell, S., Bonadonna, C., Carazzo, G., Scollo, S., Van Eaton, A. R., Taylor, I. A., Jessop, D., Eychenne, J., Gouhier, M., Mastin, L. G., Wallace, K. L., Biass, S., Bursik, M., Grainger, R. G., Jellinek, A. M., and Schmidt, A.: The Independent Volcanic Eruption Source Parameter Archive (IVESPA, version 1.0): A new observational database to support

https://doi.org/10.5194/egusphere-2026-4654
Preprint. Discussion started: 19 August 2026

explosive eruptive column model validation and development, Journal of Volcanology and Geothermal Research, 417, 107295, https://doi.org/https://doi.org/10.1016/j.jvolgeores.2021.107295, 2021.

Bednarz, E. M., Maycock, A. C., Abraham, N. L., Braesicke, P., Dessens, O., and Pyle, J. A.: Future Arctic ozone recovery: the importance of chemistry and dynamics, Atmos. Chem. Phys., 16, 12159–12176, https://doi.org/10.5194/acp-16-12159-2016, 2016.

Bellamy, R.: Responsible research for space-based climate geoengineering, Environ Sci Policy, 172, 104213, https://doi.org/https://doi.org/10.1016/j.envsci.2025.104213, 2025.

Bergesen, H. O., Parmann, G., and Thommessen, Ø. B.: World Meteorological Organization (WMO), in: Year Book of International Co-operation on Environment and Development, Routledge, 233–234, 2018.

Bernath, P., Boone, C., and Crouse, J.: Wildfire smoke destroys stratospheric ozone, Science (1979), 375, 1292–1295, https://doi.org/10.1126/science.abm5611, 2022.

Biermann, F., Oomen, J., Gupta, A., Ali, S. H., Conca, K., Hajer, M. A., Kashwan, P., Kotzé, L. J., Leach, M., Messner, D., Okereke, C., Persson, Å., Potočnik, J., Schlosberg, D., Scobie, M., and VanDeveer, S. D.: Solar geoengineering: The case for an international non-use agreement, WIREs Climate Change, 13, e754, https://doi.org/https://doi.org/10.1002/wcc.754, 2022.

Bordi, I., Berrilli, F., and Pietropaolo, E.: Long-term response of stratospheric ozone and temperature to solar variability, Ann Geophys, 33, 267–277, https://doi.org/10.5194/angeo-33-267-2015, 2015.

Bornman, J. F., Barnes, P. W., Robinson, S. A., Ballaré, C. L., Flint, S. D., and Caldwell, M. M.: Solar ultraviolet radiation and ozone depletion-driven climate change: effects on terrestrial ecosystems, Photochemical & Photobiological Sciences, 14, 88–107, https://doi.org/10.1039/c4pp90034k, 2015.

Bronsther, J. and Xu, Y.: The social costs of solar radiation management, npj Climate Action, 4, 69, https://doi.org/10.1038/s44168-025-00273-y, 2025.

Budyko, M. I.: Front Matter, https://doi.org/https://doi.org/10.1029/SP010, 1977.

Cherry, T. L., Kroll, S., McEvoy, D. M., Campoverde, D., and Moreno-Cruz, J.: Climate cooperation in the shadow of solar geoengineering: an experimental investigation of the moral hazard conjecture, Env Polit, 32, 362–370, https://doi.org/10.1080/09644016.2022.2066285, 2023.

Cicerone, R. J.: Changes in stratospheric ozone, Science (1979), 237, 35–42, 1987.

Crutzen, P. J. and Arnold, F.: Nitric acid cloud formation in the cold Antarctic stratosphere: a major cause for the springtime 'ozone hole,' Nature, 324, 651–655, https://doi.org/10.1038/324651a0, 1986.

Crutzen, P. J.: Albedo Enhancement by Stratospheric Sulfur Injections: A Contribution to Resolve a Policy Dilemma?, Clim Change, 77, 211–220, https://doi.org/10.1007/s10584-006-9101-y, 2006.

Danabasoglu, G., Lamarque, J. -F., Bacmeister, J., Bailey, D. A., DuVivier, A. K., Edwards, J., Emmons, L. K., Fasullo, J., Garcia, R., Gettelman, A., Hannay, C., Holland, M. M., Large, W. G., Lauritzen, P. H., Lawrence, D. M., Lenaerts, J. T. M., Lindsay, K., Lipscomb, W. H., Mills, M. J., Neale, R., Oleson, K. W., Otto-Bliesner, B., Phillips, A. S., Sacks, W., Tilmes, S., van Kampenhout, L., Vertenstein, M., Bertini, A., Dennis, J., Deser, C., Fischer, C., Fox-Kemper, B., Kay, J. E., Kinnison, D., Kushner, P. J., Larson, V. E., Long, M. C., Mickelson, S., Moore, J. K., Nienhouse, E., Polvani, L., Rasch, P. J., and Strand, W. G.: The Community Earth System Model Version 2 (CESM2), J Adv Model Earth Syst, 12, https://doi.org/10.1029/2019MS001916, 2020.

Domeisen, D. I. V. and Butler, A. H.: Stratospheric drivers of extreme events at the Earth's surface, https://doi.org/10.1038/s43247-020-00060-z, 1 December 2020.

Dykema, J. A., Keith, D. W., Anderson, J. G., and Weisenstein, D.: Stratospheric controlled perturbation experiment: a small-scale experiment to improve understanding of the risks of solar geoengineering, Philosophical Transactions of the Royal Society A: Mathematical, Physical and Engineering Sciences, 372, 20140059, https://doi.org/10.1098/rsta.2014.0059, 2014.

Eyring, V., Cionni, I., Lamarque, J. F., Akiyoshi, H., Bodeker, G. E., Charlton-Perez, A. J., Frith, S. M., Gettelman, A., Kinnison, D. E., Nakamura, T., Oman, L. D., Pawson, S., and Yamashita, Y.: Sensitivity of 21st century stratospheric ozone to greenhouse gas scenarios, Geophys Res Lett, 37, https://doi.org/https://doi.org/10.1029/2010GL044443, 2010.

Eyring, V., Bony, S., Meehl, G. A., Senior, C. A., Stevens, B., Stouffer, R. J., and Taylor, K. E.: Overview of the Coupled Model Intercomparison Project Phase 6 (CMIP6) experimental design and organization, Geosci Model Dev, 9, 1937–1958, https://doi.org/10.5194/gmd-9-1937-2016, 2016.

Errera, Q., Flunger, J., Funke, B., Hoffmann, A., Höpfner, M., Raspollini, P., Ungermann, J., and Sinnhuber, B.-M.: Climatology of middle atmospheric conditions to support studies of future satellite middle atmospheric missions, EGU General Assembly 2026, Vienna, Austria, 3–8 May 2026, EGU26-19902, https://doi.org/10.5194/egusphere-egu26-19902, 2026.

Fahey, D. W., Kawa, S. R., Woodbridge, E. L., Tin, P., Wilson, J. C., Jonsson, H. H., Dye, J. E., Baumgardner, D., Borrmann, S., Toohey, D. W., Avallone, L. M., Proffitt, M. H., Margitan, J., Loewenstein, M., Podolske, J. R., Salawitch, R. J., Wofsy, S. C., Ko, M. K. W., Anderson, D. E., Schoeber, M. R., and Chan, K. R.: In situ measurements constraining the role of sulphate aerosols in mid-latitude ozone depletion, Nature, 363, 509–514, https://doi.org/10.1038/363509a0, 1993.

Farman, J. C., Gardiner, B. G., and Shanklin, J. D.: Large losses of total ozone in Antarctica reveal seasonal ClOx/NOx interaction, Nature, 315, 207–210, https://doi.org/10.1038/315207a0, 1985.

Franke, H., Niemeier, U., and Visioni, D.: Differences in the quasi-biennial oscillation response to stratospheric aerosol modification depending on injection strategy and species, Atmos Chem Phys, 21, 8615–8635, https://doi.org/10.5194/acp-21-8615-2021, 2021.

Funke, B., Höpfner, M., Bender, S., Errera, Q., Grabowski, U., Hoffmann, A., Liu, H.-L., Pedatella, N. M., Raspollini, P., Ungermann, J., and Sinnhuber, B.-M.: Linear tomographic retrieval characterisation and performance estimation for the ESA Earth Explorer 11 candidate CAIRT (Changing Atmosphere Infra-Red Tomography explorer), Submitted to Atmos. Meas. Tech., 2026.

https://doi.org/10.5194/egusphere-2026-4654
Preprint. Discussion started: 19 August 2026

Gettelman, A., Mills, M. J., Kinnison, D. E., Garcia, R. R., Smith, A. K., Marsh, D. R., Tilmes, S., Vitt, F., Bardeen, C. G., McInerny, J., Liu, H. -L., Solomon, S. C., Polvani, L. M., Emmons, L. K., Lamarque, J. -F., Richter, J. H., Glanville, A. S., Bacmeister, J. T., Phillips, A. S., Neale, R. B., Simpson, I. R., DuVivier, A. K., Hodzic, A., and Randel, W. J.: The Whole Atmosphere Community Climate Model Version 6 (WACCM6), Journal of Geophysical Research: Atmospheres, 124, 12380–12403, https://doi.org/10.1029/2019JD030943, 2019a.

Gettelman, A., Mills, M. J., Kinnison, D. E., Garcia, R. R., Smith, A. K., Marsh, D. R., Tilmes, S., Vitt, F., Bardeen, C. G., McInerny, J., Liu, H. -L., Solomon, S. C., Polvani, L. M., Emmons, L. K., Lamarque, J. -F., Richter, J. H., Glanville, A. S., Bacmeister, J. T., Phillips, A. S., Neale, R. B., Simpson, I. R., DuVivier, A. K., Hodzic, A., and Randel, W. J.: The Whole Atmosphere Community Climate Model Version 6 (WACCM6), Journal of Geophysical Research: Atmospheres, 124, 12380–12403, https://doi.org/10.1029/2019JD030943, 2019b.

Griffiths, P. T., Keeble, J., Shin, Y. M., Abraham, N. L., Archibald, A. T., and Pyle, J. A.: On the Changing Role of the Stratosphere on the Tropospheric Ozone Budget: 1979–2010, Geophys Res Lett, 47, e2019GL086901, https://doi.org/https://doi.org/10.1029/2019GL086901, 2020.

Günther, A., Höpfner, M., Sinnhuber, B.-M., Griessbach, S., Deshler, T., von Clarmann, T., and Stiller, G.: MIPAS observations of volcanic sulfate aerosol and sulfur dioxide in the stratosphere, Atmos. Chem. Phys., 18, 1217–1239, https://doi.org/10.5194/acp-18-1217-2018, 2018.

Helwegen, K. G., Wieners, C. E., Frank, J. E., and Dijkstra, H. A.: Complementing CO_2 emission reduction by solar radiation management might strongly enhance future welfare, Earth System Dynamics, 10, 453–472, https://doi.org/10.5194/esd-10-453-2019, 2019.

Hubert, D., Lambert, J.-C., Verhoelst, T., Granville, J., Keppens, A., Baray, J.-L., Bourassa, A. E., Cortesi, U., Degenstein, D. A., Froidevaux, L., Godin-Beekmann, S., Hoppel, K. W., Johnson, B. J., Kyrölä, E., Leblanc, T., Lichtenberg, G., Marchand, M., McElroy, C. T., Murtagh, D., Nakane, H., Portafaix, T., Querel, R., Russell III, J. M., Salvador, J., Smit, H. G. J., Stebel, K., Steinbrecht, W., Strawbridge, K. B., Stübi, R., Swart, D. P. J., Taha, G., Tarasick, D. W., Thompson, A. M., Urban, J., van Gijsel, J. A. E., Van Malderen, R., von der Gathen, P., Walker, K. A., Wolfram, E., and Zawodny, J. M.: Ground-based assessment of the bias and long-term stability of 14 limb and occultation ozone profile data records, Atmos. Meas. Tech., 9, 2497–2534, https://doi.org/10.5194/amt-9-2497-2016, 2016.

Höpfner M., Funke, B., Bender, S., Errera, Q., Sinnhuber, B.-M., Ungermann, J., D-04-01 CAIRT linear SWB ATBDD14-4-README-3, CAIRT PerRec, 2025.

Höpfner, M.: Study on the impact of polar stratospheric clouds on high resolution mid-IR limb emission spectra, J. Quant. Spectrosc. Radiat. Transf., 83, 93–107, https://doi.org/10.1016/S0022-4073(02)00299-6, 2004.

Höpfner, M. and Emde, C.: Comparison of single and multiple scattering approaches for the simulation of limb-emission observations in the mid-IR, J. Quant. Spectrosc. Radiat. Transf., 91, 275–285, https://doi.org/10.1016/j.jqsrt.2004.05.066, 2005.

https://doi.org/10.5194/egusphere-2026-4654
Preprint. Discussion started: 19 August 2026

IPCC, Climate Change 2021 – The Physical Science Basis: Working Group I Contribution to the Sixth Assessment Report of the Intergovernmental Panel on Climate Change, Cambridge University Press, Cambridge, https://doi.org/DOI: 10.1017/9781009157896, 2023.

Kidston, J., Scaife, A. A., Hardiman, S. C., Mitchell, D. M., Butchart, N., Baldwin, M. P., and Gray, L. J.: Stratospheric influence on tropospheric jet streams, storm tracks and surface weather, Nat Geosci, 8, 433–440, https://doi.org/10.1038/ngeo2424, 2015.

Legg, S.: IPCC, 2021: Climate Change 2021 - the Physical Science basis, Interaction, 49, 44–45, 2021.

Madronich, S., Sulzberger, B., Longstreth, J. D., Schikowski, T., Andersen, M. P. S., Solomon, K. R., and Wilson, S. R.: Changes in tropospheric air quality related to the protection of stratospheric ozone in a changing climate, Photochemical & Photobiological Sciences, 22, 1129–1176, https://doi.org/10.1007/s43630-023-00369-6, 2023.

McCormick, M. P., Thomason, L. W., and Trepte, C. R.: Atmospheric effects of the Mt Pinatubo eruption, Nature, 373, 399–404, https://doi.org/10.1038/373399a0, 1995.

Mills, M. J., Richter, J. H., Tilmes, S., Kravitz, B., MacMartin, D. G., Glanville, A. A., Tribbia, J. J., Lamarque, J.-F., Vitt, F., Schmidt, A., Gettelman, A., Hannay, C., Bacmeister, J. T., and Kinnison, D. E.: Radiative and Chemical Response to Interactive Stratospheric Sulfate Aerosols in Fully Coupled CESM1(WACCM), Journal of Geophysical Research: Atmospheres, 122, 13, 13–61, 78, https://doi.org/https://doi.org/10.1002/2017JD027006, 2017.

Müller, R., Grooß, J.-U., Zafar, A. M., Robrecht, S., and Lehmann, R.: The maintenance of elevated active chlorine levels in the Antarctic lower stratosphere through HCl null cycles, Atmos Chem Phys, 18, 2985–2997, https://doi.org/10.5194/acp-18-2985-2018, 2018.

Neu, J. L., Flury, T., Manney, G. L., Santee, M. L., Livesey, N. J., and Worden, J.: Tropospheric ozone variations governed by changes in stratospheric circulation, Nat Geosci, 7, 340–344, https://doi.org/10.1038/ngeo2138, 2014.

Niemeier, U. and Schmidt, H.: Changing transport processes in the stratosphere by radiative heating of sulfate aerosols, Atmos Chem Phys, 17, 14871–14886, https://doi.org/10.5194/acp-17-14871-2017, 2017.

Nowack, P. J., Abraham, N. L., Braesicke, P., and Pyle, J. A.: Stratospheric ozone changes under solar geoengineering: implications for UV exposure and air quality, Atmos Chem Phys, 16, 4191–4203, https://doi.org/10.5194/acp-16-4191-2016, 2016.

O'Neill, B. C., Tebaldi, C., van Vuuren, D. P., Eyring, V., Friedlingstein, P., Hurtt, G., Knutti, R., Kriegler, E., Lamarque, J.-F., Lowe, J., Meehl, G. A., Moss, R., Riahi, K., and Sanderson, B. M.: The Scenario Model Intercomparison Project (ScenarioMIP) for CMIP6, Geosci Model Dev, 9, 3461–3482, https://doi.org/10.5194/gmd-9-3461-2016, 2016.

Pinto, I., Jack, C., Lennard, C., Tilmes, S., and Odoulami, R. C.: Africa's Climate Response to Solar Radiation Management With Stratospheric Aerosol, Geophys Res Lett, 47, e2019GL086047, https://doi.org/https://doi.org/10.1029/2019GL086047, 2020.

https://doi.org/10.5194/egusphere-2026-4654
Preprint. Discussion started: 19 August 2026

Preston, C. J.: Ethics and geoengineering: reviewing the moral issues raised by solar radiation management and carbon dioxide removal, WIREs Climate Change, 4, 23–37, https://doi.org/10.1002/wcc.198, 2013.

Richter, J. H., Tilmes, S., Mills, M. J., Tribbia, J. J., Kravitz, B., MacMartin, D. G., Vitt, F., and Lamarque, J.: Stratospheric Dynamical Response and Ozone Feedbacks in the Presence of SO_2 Injections, Journal of Geophysical Research: Atmospheres, 122, https://doi.org/10.1002/2017JD026912, 2017.

Ridley, D. A., Solomon, S., Barnes, J. E., Burlakov, V. D., Deshler, T., Dolgii, S. I., Herber, A. B., Nagai, T., Neely, R. R., Nevzorov, A. V., Ritter, C., Sakai, T., Santer, B. D., Sato, M., Schmidt, A., Uchino, O., and Vernier, J. P.: Total volcanic stratospheric aerosol optical depths and implications for global climate change, Geophys Res Lett, 41, 7763–7769, https://doi.org/10.1002/2014GL061541, 2014.

Riese, M., Ploeger, F., Rap, A., Vogel, B., Konopka, P., Dameris, M., and Forster, P.: Impact of uncertainties in atmospheric mixing on simulated UTLS composition and related radiative effects, Journal of Geophysical Research: Atmospheres, 117, https://doi.org/10.1029/2012JD017751, 2012.

Rodgers, C. D.: Inverse methods for atmospheric sounding: theory and practice, World Scientific, Singapore, 2000.

Russell, L. M., Rasch, P. J., Mace, G. M., Jackson, R. B., Shepherd, J., Liss, P., Leinen, M., Schimel, D., Vaughan, N. E., Janetos, A. C., Boyd, P. W., Norby, R. J., Caldeira, K., Merikanto, J., Artaxo, P., Melillo, J., and Morgan, M. G.: Ecosystem Impacts of Geoengineering: A Review for Developing a Science Plan, Ambio, 41, 350–369, https://doi.org/10.1007/s13280-012-0258-5, 2012.

Salawitch, R. J., Smith, J. B., Selkirk, H., Wargan, K., Chipperfield, M. P., Hossaini, R., Levelt, P. F., Livesey, N. J., McBride, L. A., Millán, L. F., Moyer, E., Santee, M. L., Schoeberl, M. R., Solomon, S., Stone, K., and Worden, H. M.: The Imminent Data Desert: The Future of Stratospheric Monitoring in a Rapidly Changing World, Bull Am Meteorol Soc, 106, E540–E563, https://doi.org/10.1175/BAMS-D-23-0281.1, 2025.

Santer, B. D., Bonfils, C., Painter, J. F., Zelinka, M. D., Mears, C., Solomon, S., Schmidt, G. A., Fyfe, J. C., Cole, J. N. S., Nazarenko, L., Taylor, K. E., and Wentz, F. J.: Volcanic contribution to decadal changes in tropospheric temperature, Nat Geosci, 7, 185–189, https://doi.org/10.1038/ngeo2098, 2014.

Sellitto, P., Podglajen, A., Belhadji, R., Boichu, M., Carboni, E., Cuesta, J., Duchamp, C., Kloss, C., Siddans, R., Bègue, N., Blarel, L., Jegou, F., Khaykin, S., Renard, J.-B., and Legras, B.: The unexpected radiative impact of the Hunga Tonga eruption of 15th January 2022, Commun Earth Environ, 3, 288, https://doi.org/10.1038/s43247-022-00618-z, 2022.

Sellitto, P., Kosary, M., Höpfner, M., Funke, B., Hoffmann, A., Ungermann, J., Errera, Q., Tilmes, S., and Sinnhuber, B.-M.: The enhanced capabilities of mid-infrared limb emission sounding to observe stratospheric aerosol injection geoengineering interventions, EGUsphere [preprint], https://doi.org/10.5194/egusphere-2026-919, 2026.

Sinnhuber, B.-M. et al.: The Changing-Atmosphere Infrared Tomography Explorer CAIRT – an infrared limb-imaging satellite concept to chart the middle atmosphere in the climate system, Bull. Am. Meteorol. Soc., 2026.

https://doi.org/10.5194/egusphere-2026-4654
Preprint. Discussion started: 19 August 2026

Sofieva, V. F., Szelag, M. E., Kramarova, N. A., Damadeo, R., Steinbrecht, W., Petropavlovskikh, I., Vigouroux, C., Maillard Barras, E., Zawada, D., Tourpali, K., Frith, S. M., Wild, J. D., Davis, S. M., Arosio, C., Weber, M., Rozanov, A., Auffarth, B., Froidevaux, L., Fuller, R., Degenstein, D., Dube, K., Effertz, P., Leblanc, T., Ancellet, G., Godin-Beekmann, S., McConville, G., Querel, R., Smale, D., DeBacker, M.-R., Mahieu, E., and Sussmann, R.: Updated global and regional trends of stratospheric ozone profiles, Atmos. Chem. Phys., 26, 7387–7405, https://doi.org/10.5194/acp-26-7387-2026, 2026.

Solomon, S.: Stratospheric ozone depletion: A review of concepts and history, Reviews of Geophysics, 37, 275–316, https://doi.org/https://doi.org/10.1029/1999RG900008, 1999.

Solomon, S., Garcia, R. R., Rowland, F. S., and Wuebbles, D. J.: On the depletion of Antarctic ozone, Nature, 321, 755–758, https://doi.org/10.1038/321755a0, 1986.

Solomon, S., Rosenlof, K. H., Portmann, R. W., Daniel, J. S., Davis, S. M., Sanford, T. J., and Plattner, G.-K.: Contributions of Stratospheric Water Vapor to Decadal Changes in the Rate of Global Warming, Science (1979), 327, 1219–1223, https://doi.org/10.1126/science.1182488, 2010.

Solomon, S., Daniel, J. S., Neely, R. R., Vernier, J.-P., Dutton, E. G., and Thomason, L. W.: The Persistently Variable "Background" Stratospheric Aerosol Layer and Global Climate Change, Science (1979), 333, 866–870, https://doi.org/10.1126/science.1206027, 2011.

Tie, X. and Brasseur, G.: The response of stratospheric ozone to volcanic eruptions: Sensitivity to atmospheric chlorine loading, Geophys Res Lett, 22, 3035–3038, https://doi.org/https://doi.org/10.1029/95GL03057, 1995.

Tilmes, S., Müller, R., Engel, A., Rex, M., and Russell, J. M.: Chemical ozone loss in the Arctic and Antarctic stratosphere between 1992 and 2005, Geophys. Res. Lett., 33, https://doi.org/10.1029/2006GL026925, 2006.

Tilmes, S., Sanderson, B. M., and O'Neill, B. C.: Climate impacts of geoengineering in a delayed mitigation scenario, Geophys Res Lett, 43, 8222–8229, https://doi.org/https://doi.org/10.1002/2016GL070122, 2016.

Tilmes, S., Richter, J. H., Mills, M. J., Kravitz, B., MacMartin, D. G., Vitt, F., Tribbia, J. J., and Lamarque, J.-F.: Sensitivity of Aerosol Distribution and Climate Response to Stratospheric SO2 Injection Locations, Journal of Geophysical Research: Atmospheres, 122, 12, 512–591, 615, https://doi.org/https://doi.org/10.1002/2017JD026888, 2017.

Tilmes, S., Richter, J. H., Mills, M. J., Kravitz, B., MacMartin, D. G., Garcia, R. R., Kinnison, D. E., Lamarque, J., Tribbia, J., and Vitt, F.: Effects of Different Stratospheric SO_2 Injection Altitudes on Stratospheric Chemistry and Dynamics, Journal of Geophysical Research: Atmospheres, 123, 4654–4673, https://doi.org/10.1002/2017JD028146, 2018.

Tilmes, S., MacMartin, D. G., Lenaerts, J. T. M., van Kampenhout, L., Muntjewerf, L., Xia, L., Harrison, C. S., Krumhardt, K. M., Mills, M. J., Kravitz, B., and Robock, A.: Reaching 1.5 and 2.0 °C global surface temperature targets using stratospheric aerosol geoengineering, Earth System Dynamics, 11, 579–601, https://doi.org/10.5194/esd-11-579-2020, 2020.

https://doi.org/10.5194/egusphere-2026-4654
Preprint. Discussion started: 19 August 2026

Tilmes, S., Richter, J. H., Kravitz, B., MacMartin, D. G., Glanville, A. S., Visioni, D., Kinnison, D. E., and Müller, R.: Sensitivity of Total Column Ozone to Stratospheric Sulfur Injection Strategies, Geophys Res Lett, 48, https://doi.org/10.1029/2021GL094058, 2021.

Tilmes, S., Visioni, D., Jones, A., Haywood, J., Séférian, R., Nabat, P., Boucher, O., Bednarz, E. M., and Niemeier, U.: Stratospheric ozone response to sulfate aerosol and solar dimming climate interventions based on the G6 Geoengineering Model Intercomparison Project (GeoMIP) simulations, Atmos Chem Phys, 22, 4557–4579, https://doi.org/10.5194/acp-22-4557-2022, 2022.

Visioni, D., Pitari, G., and Aquila, V.: Sulfate geoengineering: a review of the factors controlling the needed injection of sulfur dioxide, Atmos Chem Phys, 17, 3879–3889, https://doi.org/10.5194/acp-17-3879-2017, 2017.

Xia, Y., Hu, Y., Huang, Y., Bian, J., Zhao, C., Lin, J., Xie, F., and Zhou, C.: Stratospheric Ozone Loss Enhances Summer Precipitation Over the Southern Slope of the Tibetan Plateau, Geophys Res Lett, 50, https://doi.org/10.1029/2023GL103742, 2023.

Von Clarmann, T., Degenstein, D. A., Livesey, N. J., Bender, S., Braverman, A., Butz, A., Compernolle, S., Damadeo, R., Dueck, S., Eriksson, P., Funke, B., Johnson, M. C., Kasai, Y., Keppens, A., Kleinert, A., Kramarova, N. A., Laeng, A., Langerock, B., Payne, V. H., Rozanov, A., Sato, T. O., Schneider, M., Sheese, P., Sofieva, V., Stiller, G. P., von Savigny, C., and Zawada, D.: Overview: Estimating and reporting uncertainties in remotely sensed atmospheric composition and temperature, Atmos. Meas. Tech., 13, 4393–4436, https://doi.org/10.5194/amt-13-4393-2020, 2020.

Zhang, Y., Cooper, O. R., Gaudel, A., Thompson, A. M., Nédélec, P., Ogino, S.-Y., and West, J. J.: Tropospheric ozone change from 1980 to 2010 dominated by equatorward redistribution of emissions, Nat Geosci, 9, 875–879, https://doi.org/10.1038/ngeo2827, 2016.